Hydro-morphodynamics triggered by extreme riverine floods in a mega fluvial-tidal delta

Jie Wang [a, c], Zhijun Dai [a, b,*], Sergio Fagherazzi [c], Xiaohe Zhang [c]

[a] State Key Laboratory of Estuarine and Coastal Research, East China Normal University, Shanghai 200241, China

[b] Laboratory for Marine Geology, Qingdao National Laboratory for Marine Science and Technology, Qingdao 266237, Shandong, China

[c] Department of Earth and Environment, Boston University, Boston 02215, Massachusetts, USA

[*]Corresponding author: Prof. Zhijun Dai

State Key Laboratory of Estuarine and Coastal Research, East China Normal University, Shanghai 200241, China

Email: zjdai@sklec.ecnu.edu.cn

Tel: +86 21 54836002

Fax: +86 21 54836458

Abstract:

Maintaining accretion and progradation in a mega delta is crucial to its geomorphic stability and ecology. Extreme riverine floods can disturb hydro-sediment dynamics with great damage to the deltaic landscape, as for instance deltaic erosion. Nowadays, most mega deltas suffer from sediment starvation. Understanding the impact of extreme floods is a priority to determine the long-term fate of deltaic systems. Herein, we used the Delft 3D model and field data to study the hydraulics and morphodynamics of the 2016 extreme riverine floods in the South Passage (SP) of the Yangtze Delta. Results reveal that extreme floods can increase water levels, velocities, and bed shear stresses in an inner estuarine channel and mouth bar, while the flood has a weak effect in offshore areas. High-energy floods trigger strong tidal asymmetry and Euler residual currents, which intensifies downstream suspended sediment transport and bottom riverbed erosion. In comparison with those during extreme floods in 2016, net erosion after floods passed away was generated with seaward weakened magnitudes, the corresponding mean bathymetric erosion thickness was 19.97 cm, 12.71 cm and 4.62 cm in inner estuarine channel, mouth bar and offshore area, respectively. Even though the seaward deposition patches were due to lower scouring effect and converged sediment. Hydrodynamic increments in deeper channels were more significant, while shoals and deeper areas were strongly eroded with the lowest erosion between -5 m to -6 m isobath. These results further clarified the bathymetric patterns with highlights of extreme riverine floods that can amplify the sediment-insufficient risks in such mega fluvial-tidal delta.

Keywords:

Hydrodynamics, Bathymetric changes, Extreme riverine floods, Erosion risks, Mega fluvial-tidal delta, the Yangtze Delta

1. Introduction

Estuarine deltas are dynamic zones where riverine and oceanic processes interact, leading to crucial land building, formation of important ecological environments, and storm-resistance services (Bianchi and Allison, 2009; Nienhuis et al., 2020). Riverine runoff and tidal hydrodynamics dominate sediment transport, and are more prominent in a monsoonal and meso-macrotidal deltaic system (Fettweis et al., 1998; Dalrymple and Choi, 2007; Fagherazzi et al., 2015). Extreme riverine floods in areas with a seasonal climate can cause significant interference on deltaic hydrodynamics and sediment budgets, especially in deltas with high suspended sediment concentration (SSC) and mixed stratification (Hoitink and Jay, 2016; Choi et al., 2020).

In recent decades, abundant terrigenous sediments that produced deltaic progradation have drastically declined due to anthropogenic activities in the catchment. Most global mega deltas, such as the Yangtze (Changjiang), Mississippi, Ganges-Brahmaputra and Nile Delta, have suffered for sediment starvation contributing to potentially irreversible deltaic erosion (Syvitski, 2003; Darby et al., 2016; Angamuthu et al., 2018), while water discharge delivered into the delta from upstream exhibits an almost unchanged trend (Gerten et al., 2008; Dai et al., 2018 & 2019; Best, 2019). Thereof, a sediment-hungry runoff during occasional and extreme floods could cause abnormal erosion or deposition (Cooper, 2002; Maillet et al., 20016; Allison et al., 2017; Wang et al., 2020). However, few studies have focused on the deltaic response and morphological change under such scenario..

Understanding hydro-morphodynamics triggered by high-energy riverine floods is of great significance (Edmonds and Slingerland, 2010). Extreme floods carrying low sediment loads could flush deltaic channels; while tidal pumping effect could cause a seaward net sediment deposition (Uncles, 2002; Do et al., 2020). Riverine floods will also induce large-scale sediment transport and redistribution in the maximum turbidity zone (MTZ) due to the blocking effect of mouth bars (van Maren and Hoekstra, 2004; Boudet et al., 2017).

Longitudinally, the inner estuarine channel upstream of the mouth bar is dominated by riverine floods, while offshore areas are affected by tidal forcing (Azhikodan and Yokoyama, 2019). Under extreme riverine floods, the scouring potential of the flow current will be significantly enhanced (Kitheka et al., 2005).

Lamb et al. (2012) used a 2-D hydrodynamic and sediment transport model to study the lower reaches of the Mississippi Delta, USA. They showed that the delta suffered erosion after a large flood, increasing the riverine sediment transport offshore. After the 2011 flood in the Hudson River, USA, Ralston et al. (2013a) found that the sediment transported into the lower estuary was approximately 2.70×10^6 t, about five times the usual amount. Boudet et al. (2017) utilized the Delft 3D model to explore the sediment transport pattern after flood peaks in the Rhone Delta, France, indicating that riverine sediments can always be exported to deeper deltaic areas through mouth bars and the MTZ. In the Amazon River Delta, Brazil, and Ayeyarwady Delta, Myanmar, estuarine processes can intercept part of the riverine sediment transported to the deeper subaqueous delta, and also capture some suspended sea-sourced sediment (Asp et al., 2018; Glover et al., 2021). There is a need to understand the hydrodynamics and sediment transport in estuarine deltas with high turbidity, with a particular emphasis on extreme floods in a sediment starvation condition. Scarce information is available on the response of the Yangtze Delta to extreme floods.

The Yangtze Delta is a mega mixed fluvial-tidal delta located on the east coast of Asia (Fig. 1a), its hydro-morphodynamics is deeply influenced by multiple natural processes and human activities (Dai et al., 2014 & 2015; Wei et al., 2019). The tide is irregular and semi-diurnal with mean tidal range of 2.60 m near the Hengsha Island, while the maximum tidal range exceeds 4.6 m (Yun, 2004). During the past two millennia the delta was fed by abundant fine-grained sediments. The deposition of this material gave rise to the current geomorphic configuration with three-level bifurcations and four-outlets. Mouth bars also formed under the combined influence of runoff and tidal forcing (Chen et al., 1979 & 1999) (Fig. 1b). Between 1950 and 2015, the mean annual runoff and sediment discharge entering the estuarine part of the Yangtze delta at Datong station (the tidal limit) were up to 8.93×10^{11} m^3 and 3.68×10^8 t, with a mean SSC of 0.45 kg/m^3 (Dai et al., 2018). The SSC and sediment transport load declined in recent decades after the construction of cascade reservoirs such as the Three Gorges Dam (TGD) in 2003 (the largest water conservancy project in the world). During 2000-2019, the sediment load declined by more than 70% to 1.21×10^{8} t/y, although the annual water discharge has remained stable (CWRC, 2019; Dai and Liu, 2013; Dai et al., 2018) (Fig. 1a). As a result, the sediment budget and the substrate equilibrium along the middle-lower reaches of the estuarine delta were altered. Most downstream riverbeds are at risk of insufficient sediment inputs and large-scale erosion, particularly in the inner estuarine channels (Dai et al., 2016; Luan et al., 2016; Mei et al., 2018a; Zhou et al., 2020). In the Yangtze Delta, extreme riverine floods affect erosion-deposition processes on both short-term and seasonal timescales. These floods are crucial triggers of geomorphic evolution (Wang et al., 2011; Dai et al., 2014; Fan et al., 2017; Mei et al., 2018b). Nowadays, sea-sourced sediments resuspended by tidal currents are enhanced. These sediments mitigate the decline in SSC in the MTZ of the Yangtze Delta, delaying the effect of damming with respect to other regions (Dai et al., 2013 & 2018).

Herein, the South Passage (SP) (Fig. 1b) was selected to study the effects of extreme floods. The SP is an important distributary located in the MTZ. The channel has fast accumulating shoals and a developed mouth bar (Fig. 1b). During the flood season, enhanced runoff increases the sediment-carrying capacity, water surface gradients become steeper, and tidal pumping effect is weakened (Liu et al., 2011; Zhang et al., 2018a). Such hydrodynamic environment is conducive to downstream transport of fine-grained muddy sediments (Wu et al., 2012; Li et al., 2018). Historically, the Yangtze floods in 1931, 1954, 1983 and 1998, triggered scour and shoal migration within the upstream entrance of the SP (Yun, 2004; Wei et al., 2019). In particular, in 2016 a large-scale flood occurred at the beginning of the flood season; the runoff was about twice that of a normal year, but the annual total sediment load did not increase (CWRC, 2016). In this study, the SP was selected to elucidate the hydrodynamic and morphodynamic of the South Passage during the extreme riverine flood of 2016. The main objectives of the paper are: (1) to compare the hydrodynamics of the SP during extreme riverine floods and with low runoff, (2) to explore the bathymetric erosion-deposition patterns of SP sub-reaches, (3) to quantify the impact of the flood on the sediment budget and channel morphology.

2. The South Passage

The Yangtze River is the third longest river worldwide and the largest in Asia, with a total length of 6,300 km and a drainage area of 1.90×10^6 km^2 (Fig. 1a). The middle and lower reaches of the Yangtze River are in a subtropical monsoon region. Almost 70% of the annual runoff and 80% of the sediment load are delivered to the delta during the flood season, and most sediment is deposited in the subaqueous delta and transport downstream through the South Channel (Yun, 2004; Hu et al., 2009). During the past five decades, the SSC in the Yangtze Delta showed a declined trend, especially during the flood season. Its average value has dropped to only 25% of the historical value, while water discharge has remained stable (Fig. S1).

At the transition from river-dominated to tide-dominated, salt and fresh water are fully mixed. Under significant water stratification and tidal asymmetry, both a MTZ and a mouth bar develop (Li and Zhang, 1998) (Fig. 1b). The maximum ebb velocity can reach 2 m/s in the flood season during spring tide (Yun, 2004). Within the MTZ and near the deltaic front, there are large deposits of muddy sediments with high erodibility. This material can be erode by tidal currents with high velocities. Winds and waves also affect flow velocity and bottom shear stresses, enhancing the scour of sediments in shallow areas (Shen and Pan, 2001). Hydro-morphodynamic processes in the SP have been disturbed by engineering projects, such as the Deepwater Navigation Channel Project (DNCP) and adjacent intertidal reclamations (Fig. 1b)., The SP width increases moving offshore, while interactions between runoff and tidal forcing are occurring along the entire channel length (Lu et al., 2015).

3. Data acquisitions and processing

3.1 Data acquisitions

A total of five datasets were collected. The first dataset includes riverine water discharge and SSC at Datong station. Monthly water discharge and SSC from 1971 to 2019 were used to analyze changes in riverine stage, magnitude and frequency of high runoff. As a result, four runoff levels were selected: $Q_{20,000}$, $Q_{40,000}$, $Q_{60,000}$, and $Q_{80,000}$ m^3, as different inputs to the model. They are respectively higher than 1%, 50%, 95% and 100% of the cumulative frequency of monthly water discharge that flow into delta during the flood season (May-August) (Fig. S2a). The total water discharge in 2016 was higher than any discharge in the two decades before 2020, especially in the beginning of flood season (Fig. S2b). In 2020 another flood occurred, with runoff that increased from 45,000 m^3/s to more than 80,000 m^3/s in half a month (Fig. S2b-d). Daily water discharge in 2016 was also obtained, as the prescribed inputs for the model.

The second dataset covers measured hydrodynamic data in the Yangtze Delta, including water levels, flow velocities and directions obtained at multiple observation sites (Fig. 2a). These data are used for comparison with modeled results and to evaluate model efficiency. Water levels were measured at six tidal stations in August 9-24, 2011 (neap-spring-neap cycle), these stations are distributed in the delta upper and lower channels (Fig. 2c). Flow velocities and directions were measured simultaneously during a spring tide in August 2011 at 8 fixed field sites (Fig. 2c). At each site, hourly flow velocities and directions of six water layers ($H_{0.0}$, $H_{0.2}$, $H_{0.4}$, $H_{0.5}$, $H_{0.8}$, $H_{1.0}$) were collected, using shipboard ultrasonic HXH03 Doppler current flow meters (RUNSUN, the accuracy of velocity and direction are 1 cm/s and 3°). From these data, the hourly depth-averaged flow velocity and direction can be obtained (formula 1-4).

$$V_E = \frac{1}{10}\left(V_{E\_H0.0} + 2V_{E\_H0.2} + 2V_{E\_H0.4} + 2V_{E\_H0.6} + 2V_{E\_H0.8} + V_{E\_H1.0}\right) \quad (1)$$

$$V_N = \frac{1}{10}\left(V_{N\_H0.0} + 2V_{N\_H0.2} + 2V_{N\_H0.4} + 2V_{N\_H0.6} + 2V_{N\_H0.8} + V_{N\_H1.0}\right) \quad (2)$$

$$V_{depth\_averaged} = \sqrt{{V_E}^2 + {V_N}^2} \quad (3)$$

$$D_{depth\_averaged} = arctan(V_E/V_N) \quad (4)$$

where $V_{E\_H0.0}$ and $V_{N\_H0.0}$ are eastward and northward components of the measured velocity in $H_{0.0}$, V_E and V_N are eastward and northward depth-averaged velocity, $V_{depth\_averaged}$ is depth-averaged velocity, and $D_{depth\_averaged}$ is direction of depth-averaged velocity.

The third dataset encompasses bed sediments and vertical SSC collected at five fixed sites in September 2017 (Fig. 2d). Hourly suspended water samples at 6 water depths were collected for 26 hours covering the entire flood-ebb cycle. After treatment, mean, median and maximum grain size were determined using a laser particle analyzer (Mastersizer 2000, Malvern, UK).

The fourth dataset are the bed sediment characteristics for the entire SP. Sediment fractions (silt, clay and sand) were obtained for the Yangtze Delta in 2015. sampling sites spanned the SP channel and parts of the bordering shoals. A Kriging interpolation was used to calculate the three sediment fractions along the SP. In addition, the critical erosion shear stresses (τ_{cr}) of bed sediments were obtained from the literature (Yang et al., 2017; Zhang et al, 2018; Qiao et al., 2021). The critical shear stress is about 0.67 N/m^2 along upper reach, about 0.76 N/m^2 on the outside of the mouth bar, and 0.56 N/m^2 in the deeper offshore area.

The fifth dataset includes multiple bathymetries collected in different areas. (1) For the SP, a total of 14 semiannual bathymetries in different years with a scale of 1:10,000 (Table S1) were used to analyze erosion-deposition patterns during the flood and dry season. (e.g. bottom variations after the 2016 extreme floods). Spatial density of sounding points is approximately 35-48 points/km^2, which is acceptable for geomorphic analyses (Wang et al., 2020). (2) bathymetry data of the Yangtze river channel were collected with a scale of 1:80,000 in 2012. All these data were provided by the Yangtze Delta Waterway Administration, Chinese Ministry of Transportation. The Natural Neighbor Interpolation (Sibson, 1981; Lentz and Hapke, 2011) was applied to generate digital elevation models (DEMs) of the SP and river channel in different periods, with a grid resolution of 20×20 m. (3) For the oceanic area, gridded bathymetries were obtained from GEBCO at 15 arc-second intervals (General Bathymetry Chart of the Oceans, https://www.gebco.net/). Finally, bathymetries of the entire study domain were generated and converted to mean sea level datum (Fig. 2b).

3.2 Model setup and processing

3.3.1 Model domain and boundary conditions

The 2-D Delft 3D model was applied to simulate hydrodynamics and bottom variations under different riverine runoffs. The model solves the unsteady shallow water equations with the hydrostatic pressure hypothesis, using orthogonal curvilinear coordinates (Deltares, 2014). Model domain extends from upstream Datong station to the Yellow Sea and the East China Sea at the 80 m isobath, including Hangzhou Bay (Fig. 2a). Shoreline boundaries strictly follow the actual distribution in 2016 and were extracted from Landsat images. The west-east and north-south domain sizes were approximately 700 km and 560 km, with a model grid of 1,463×507 points (Fig. 2a). The resolution of the orthogonal curvilinear grid varied from about 200 m in the inner estuary to 3,000 m at the oceanic boundary. As a result, in the SP the grid resolution is acceptable to calculate hydrodynamics. Moreover, we calculated Manning coefficients in the delta based on generated bathymetric data, the value was about 0.011-0.016, and we set a uniform Manning coefficient of 0.020 in the river channel and 0.011 in the ocean (Zhang et al., 2018b; Chu, 2019). The artificial groins and dikes of the DNCP were represented in the model by Current Deflection Wall (CDW) (Fig. 2c). The elevation of CDW was set to 0.3 m to allow flooding within adjacent waters at high tide. Time step of hydrodynamic calculation was 60 s to meet CFL criteria (Deltares, 2014).

Both landward river boundary and oceanic boundary conditions were considered in this model. First, we prescribed the measured daily water discharge in May and July 2016 and four constant values ($Q_{20,000,}$ $Q_{40,000,}$ $Q_{60,000,}$ and $Q_{80,000}$ m^3) at Datong station. A constant runoff of 1000 m^3/s was specified at the entrance of Hangzhou Bay, to represents the river input from the upstream Qiantang River (Fig. 2b). Second, at the ocean open boundary, an astronomic tidal forcing with 13 harmonic constituents was prescribed (Fig. 2b). The Constituents were extracted from the Global Tidal Models of TPXO 9.0 (https://www.tpxo.net/global), with 1/30-degree resolution. The tidal parameters were set on 19 equidistant points along the three open ocean boundaries. Possible errors caused by boundary effects are limited in such a large model domain.

We did not account for wind waves, water temperature, and salinity.

3.2.2 Model calibrations and runoff scenarios

Model results were compared to field measurements to analyze the accuracy and effectiveness of the model. Root mean square error (RMSE), correlation coefficient (CC) and model efficiency (ME) were used (formula 5-7):

$$RMSE = \sqrt{\frac{(X_{mod}-X_{obs})^2}{N}} \tag{5}$$

$$CC = \frac{\sum(X_{mod}-\overline{X}_{mod})(X_{obs}-\overline{X}_{obs})}{\left[\sum(X_{mod}-\overline{X}_{mod})^2\sum(X_{obs}-\overline{X}_{obs})^2\right]^{0.5}} \tag{6}$$

$$ME = 1 - \frac{\sum(X_{mod}-X_{obs})^2}{\sum(X_{obs}-\overline{X}_{obs})^2} \tag{7}$$

where X_{mod} and X_{obs} are the modeled result and observed data, respectively, $\overline{X}_{obs}$ is the mean of observed data. A ME>0.65 indicates excellent model performance while 0.65>ME>0.50 indicates good performance (Allen et al., 2007).

Six runoff scenarios were considered at the landward boundary, including four water discharges levels ($Q_{20,000}$, $Q_{40,000}$, $Q_{60,000}$, and $Q_{80,000}$ m^3) in July 2016, and two daily values in May and July 2016 to represent the riverine conditions at the beginning of flood season and extreme floods. Minima riverine inputs in May and July 2016 were 44,600 $m^3$and 54,000 m^3, the maxima were 49,400 m^3 and 70,100 m^3, and monthly means were 47100 m^3 and 65400 m^3, respectively. Extreme high daily runoff above 80,000 m^3/s occurred during the 1998 and 2020 catastrophic floods (Fig. S2b). All modeled hydrological scenarios were run for a month (30 days) and the output results were saved hourly.

The *RMSE* of modeled versus observed water levels in August 2011 ranges from 0.18 m to 0.28 m, *CC* are all over 0.96, and *ME* are higher than 0.89 (Fig. S3; Table S2). The Calibration of water levels is excellent, especially at stations close to the SP (Fig. S3). *RMSE* of modeled flow velocities at eight field sites are about 0.08-0.25 m/s, *ME* values indicate that modeled flow velocities are reliable except for SP2 (Fig. S4; Table S3). *RMSE* of modeled flow directions ranges from 14.70° to 39.40°, with excellent *CC* and *ME* except for SB1 (Fig. S5; Table S3).

3.2.3 Estuarine cross sections for data analysis

To better understand water transport through the distributaries, three cross-transects were set up to calculate the cumulative water discharge (Fig. 2c). The first transect (WT 1) is at the entrance of the South Branch, and represents the water flux into the entire Yangtze Delta. The second and third transects (WT 2 and WT 3) are at the uppermost and lowermost reaches of the SP, respectively (Fig. 2c). In addition, data along the SP thalweg (61 km in length) were extracted to analyze longitudinal changes in hydrodynamics. The water depth becomes shallower at the mouth bar, and then deepens shoreward (Fig. 2d-2f). Furthermore, 60 equally spaced cross sections were set up with an interval of 1 km along the SP (Fig. 2d). Mean values of hydrodynamic parameters were extracted in each cross section. Channel width gradually widens shoreward, increasing from 2.92 km at the entrance to 20.24 km at the outermost cross section (Fig. 2g). The average water depth of the cross sections is low in the upstream narrow reaches and on the month bar, and high in the uppermost and lowermost reaches (Fig. 2g). Average water level, flow velocity, bed shear stress were calculated at each cross section under different modeled scenarios.

The SP was divided in three sub-reaches according to geomorphic features and water depths along the thalweg: the inner estuarine channel, the mouth bar, and the offshore area (Fig. 2d). (1) The inner estuarine channel (0-26 km) hosts the South Jiangya Shoal and is dominated by runoff. The water depth of the thalweg gradually shallows from almost -14 m to only -7 m (Fig. 2e-2f). (2) The mouth bar (26-40 km) is the shallowest area; at the crest the depth is less than 6 m, the Jiuduansha and Nanhui Shoals and deep channel further away generate longitudinal geomorphic differentiation (Fig. 2e-2f). (3) The offshore area (40-61 km) is deeper and dominated by tidal forcing; the shoals at both sides gradually shrink, and the gradient along the thalweg increases seaward (Fig. 2e-2f).

3.2.4 Calculation of hydrodynamic parameters

Average water level, flow velocity, and bed shear stress were calculated at the cross sections along the thalweg for different scenarios. The longitudinal changes indicate relative variations between the riverine runoff and tidal forcing. The distribution of mean and maximum bed shear stress in all scenarios were also computed. The hydrodynamic impact of extreme riverine floods can be analyzed comparing the flood to low riverine inputs in the early flood season. The flood is associated to erosion-deposition patterns.

Tidal asymmetry directly affects sediment transport and morphodynamic changes in deltas. The tidal component calculation program (T_TIDE) developed by Pawlowicz et al. (2002) was used to carry out an harmonic analysis of the modeled water levels and flow velocity. In the Yangtze Delta, the tidal forcing is semi-diurnal; we applied the method of Friedrichs and Aubrey (1998) to calculate tidal asymmetry along the SP (formula 8-9):

$$A_r = \alpha_{M_4}/\alpha_{M_2} \tag{8}$$

$$G_r = 2g_{M_2} - g_{M_4} \tag{9}$$

where, α_{M_2} and α_{M_4} are the amplitudes of the M_2 and M_4 tidal constituents, g_{M_2} and g_{M_4} are the phases of the M_2 and M_4 constituents, A_r indicates intensity of tidal deformation (significant for A_r>0.01), G_r indicates direction of tidal deformation. When 0°<G_r<180° the flow is dominated by flood tide (duration of flood tide shorter than ebb tide), when 180°<G_r<360° the ebb tide is dominant. The tidal skewness of the water level time derivative was also calculated (formula 10) (Nidzieko, 2010):

$$\gamma = \frac{\frac{1}{T-1}\sum_{t=1}^{T}(x_t-\overline{x})^3}{\left[\frac{1}{T-1}\sum_{t=1}^{T}(x_t-\overline{x})^2\right]^{3/2}} \tag{10}$$

where x_t is the derivative of water level with respect to time, $\overline{x}$ is the mean water level. γ<0 indicates ebb-dominance, while γ>0 indicates flood-dominance.

Moreover, residual currents can characterize the direction and intensity of water-sediment transport by the average tidal currents (Dyer, 1973). Euler residual currents in January, May and July of 2016 were calculated, using the average current vectors of two flood-ebb tidal cycles during spring tide (26 hours).

3.2.5 Bathymetric changes

Bathymetric erosion-deposition patterns were obtained by subtracting two subsequent DEMs, (Mei et al., 2018b) (formula 11).

$$\Delta h(x, y, t_1, t_2) = h_2(x, y, t_2) - h_1(x, y, t_1) \quad (11)$$

where $h_1(x, y, t_1)$ and $h_2(x, y, t_2)$ are riverbed elevations at any position (x, y) at times t_1 and t_2. Area/volume of erosion/deposition can be calculated during a certain period. In this study, we focused on the bathymetric changes during the 2016 flood season from May to August after the extreme floods. The erosion-deposition magnitudes at different water depths were also identified. Moreover, the geomorphic adjustments during other periods were considered as the basis for further discussions.

4. Results

4.1 Hydrodynamics under low runoff

In the $Q_{20,000}$ scenario, the mean water level computed by the model is about 0.16 m at the upstream entrance and declines downstream along the thalweg, the water slope is high near the South Jiangya Shoal (Fig. 3a). The depth-averaged velocity rapidly increases from 0.97 m/s to 1.19 m/s when the channel narrows, and then decreases to less than 0.8 m/s in the offshore area (Fig. 3a). The trend in average bed shear stress is consistent with the flow velocity, with a peak of 0.84 N/m^2 in the inner estuarine channel and values of 0.67 N/m^2 and 0.50 N/m^2 in the mouth bar and offshore area, respectively (Fig. 3b). The bed shear stress angle rotates southward moving downstream (Fig. 3b). The values along the thalweg are then compared to the average values computed along the cross sections 1 to 60. The mean water level averaged in each cross section also decreases seaward with two secondary peaks, and the depth-averaged flow velocity decreases rapidly on the mouth bar (transect 26 to 40) from 0.89-0.95 m/s to 0.72-0.76 m/s (Fig. 3c). The mean bed shear stress increases sharply from about 0.56 N/m^2 to the maximum of 0.80 N/m^2 on the mouth bar, and then drops to 0.38 N/m^2 in the offshore area (Fig. 3d).

In the $Q_{20,000}$ scenario, the areas with a mean bed shear stress higher than 0.7 N/m^2

($\tau_{>0.7}$) are distributed along the inner estuarine channel, especially in the narrow and shallow reaches (Fig. 3e). The total area with $\tau_{>0.7}$ is 123.63 km^2, accounting for 16.57% of the SP (Table 1). The area of $\tau_{>0.5}$ extends offshore with a protruding shape (Fig. 3e). In terms of maximum bed shear stress in a tidal cycle, areas with $\tau_{>2.8}$ are also located along the inner estuarine channel and partly penetrate the mouth bar with a total area of 98.29 km^2 (Fig. 3f). There is a secondary area of high bed shear stress in the channel that connects the mouth bar with the coastal ocean, where the flow accelerates again (Fig. 3f). The frequency distribution of mean bed shear stress has a peak at 0.40-0.70 N/m^2 (Fig. S6a), while the frequency distribution of maximum bed shear stress has a peak of 1.10-1.30 N/m^2 (Fig. S6b).

An harmonic analysis of the $Q_{20,000}$ scenario indicates that the M2 constituent propagates upstream and slightly increases of 3.16 cm until km 45, and then weakens almost linearly of 35.24 cm in the inner estuarine channel (Fig. S7a). On the contrary, the M4 amplitude progressively increases in the channel (Fig. S7b). Therefore the tidal asymmetry (M4/M2) increases landward and the variation gradient is largest in the middle reaches (Fig. 3g). The water level phase of the M2 and M4 constituents increase upstream (Fig. S7c-S7d). The phase difference (2M2-M4) is between 0°-180° (the difference minimum is reached on the mouth bar), which indicates that the tidal asymmetry is flood-dominant (Fig. 3g). Moreover, the velocity amplitudes of both M2 and M4 increase in the narrow channel that borders the South Jiangya Shoal and then decrease downstream; the corresponding ratio decreases sharply and remains stable (Fig. S8a-S8b and 3h).

4.2 Hydrodynamics under moderate runoff

Under moderate riverine runoff (Q=40,000 m^3/s), the mean water level is higher along the thalweg and maintains a similar longitudinal trend (Fig. 4a). The higher runoff also results in faster flow velocity in the SP: the overall average velocity increases to 0.98 m/s (Fig. 4a). A higher runoff also causes stronger bed shear stress (average of 0.76 N/m^2), with the largest increase in the upstream channel, with lower angles that direct the flow more towards downstream (Fig. 4b). In particular, the average value of mean bed shear stress in the inner estuarine channel is 27.81% higher than that on the mouth bar and 80.65% higher than the value in the offshore area (Fig. 4b). Overall, the hydrodynamic variations from cross section 1 to transect 60 are similar to that along the thalweg, higher runoff input leads to higher velocity and water level and their magnitude gradually weakens downstream (Fig. 4c-4d). Specifically, the average values of mean water level, mean flow velocity and mean bed shear stress are 43.89%, 10.83% and 4.27% higher than that under $Q_{20,000}$ scenario, and the angle of bed shear stress is 1.59° lower (Fig. 4c-4d).

The area of $\tau_{>0.7}$ increases to 142.47 km^2 (19.10% to the entire SP) and fully covers the inner estuarine channel and expands to most of the mouth bar (Table 1; Fig. 4e), the upstream area with values higher than 0.90 N/m^2 increases significantly (Fig. 4e and S6a). Moreover, the area with $\tau_{>0.5}$ has gradually changed shape in a smooth-blunted pattern (Fig. 4e). The area with a high value of maximum bed shear stress has also moved offshore; the area with $\tau_{>2.8}$ increases to 142.07 km^2 from 98.29 km^2 under the $Q_{20,000}$ scenario (Table 1; Fig. 4f). There is still an area of lower maximum shear stress on the crest of the mouth bar (Fig. 4f and S6b).

The tidal harmonic analysis shows that as the runoff input increases, the M4 constituent of water level decreases and the M2 constituent increases more toward upstream (Fig. S7a-S7b). Therefore, tidal asymmetry is enhanced upstream and it is related to an increase in tidal energy transfer, while the asymmetry in the offshore area is small (Fig. 4g). The phase difference of water level under higher runoff increases in the offshore area, however, decreases in inner estuarine channel (Fig. 4g). As for the flow velocity, amplitude ratio and phase difference both decreases, and the variation is greater in the upstream channel (Fig. 4h).

4.3 Hydrodynamics under extreme floods

In the $Q_{60,000}$ and $Q_{80,000}$ scenarios the mean water level along the thalweg significantly increases, and the enhancement is the largest in the inner estuarine channel

(Fig. 5a). From the $Q_{20,000}$ scenario to $Q_{80,000}$ scenario, the overall average value of water level increases from 0.07 m to 0.18 m, with an increase in the upstream entrance of 0.22 m, but with an increase of only 0.02 m in the most downstream cross section (Fig. 5a). Flow velocity is also enhanced, the average value in three sub-reaches is 1.19 m/s, 1.00 m/s and 0.94 cm/s, respectively. The largest increase is concentrated in inner estuarine channel after the restriction of the South Jiangya Shoal (Fig. 5a). Moreover, the variation trend of mean bed shear stress is basically the same as mean velocity, its average under $Q_{80,000}$ scenario is 0.87 N/m^2, 23.65% higher than that of $Q_{20,000}$ scenario; the average in the inner estuarine channel is larger than on the mouth bar and in the offshore area by 13.83% and 78.33% (Fig. 5b). Overall, extreme floods cause greater scouring hydrodynamics in the upstream estuarine channel (Fig. 5a-5b).

The mean water level shows consistent trends in the cross sections 1 to 60. From the $Q_{20,000}$ to the $Q_{80,000}$ scenario, the water level increases by 129.61%, 100.91% and 10.26% in the inner estuarine channel, mouth bar and offshore area, respectively (Fig. 5c). Correspondingly, the average value of flow velocity increases by 7.28%, 5.77% and 0.38%, respectively (Fig. 5c). The extreme runoff also generates higher bed shear stress, with a percentage increase of 20.34% and 17.30% in inner estuarine channel and mouth bar. The increase is lower in the nearshore area (4.81%) (Fig. 5d). The average angle of bed shear stress at all cross sections is also slightly reduced under extreme floods (Fig. 5d).

Significantly, for mean bed shear stress, the area of $\tau_{>0.7}$ increases to 185.28 km^2 under $Q_{60,000}$ scenario and 229.56 km^2 under $Q_{80,000}$ scenario (Fig. 5e1-5e2). The high-stress area continues to develop along the inner estuarine channel and crosses the mouth bar, however, its enhancement in the tails of the South Jiangya and Jiuduansha Shoal is limited (Fig. 5e1-5e2). Comparing both $Q_{80,000}$ and $Q_{20,000}$ scenario, area with $\tau_{>0.8}$, $\tau_{>0.7}$, $\tau_{>0.6}$ *and* $\tau_{>0.5}$ seaward moves 8.13 km, 12.79 km, 3.18 km and 1.56 km, respectively (Fig. 5e1-5e2). The maximum bed shear stress is also greatly enhanced and area of $\tau_{>2.8}$ increases from 98.29 km^2 ($Q_{20,000}$) to 231.54 km^2 under ($Q_{80,000}$) (Fig. 5f1-5f2). Areas with high bed shear stress move offshore and the two peak areas gradually merge in the $Q_{80,000}$ scenario;, however, the difference in bed shear stress is relatively weak in the offshore area (Fig. 5f1-5f2).

Under extreme floods, the amplitude of the M2 constituents of water level decreases along the thalweg while the M4 increases (Fig. S7a-S7b). In the upstream channel the tidal asymmetry increases more significantly, while is weak in the offshore area (Fig. 5g). The phase difference of 2M2-M4 increases in the upstream channel and in the offshore area, while it becomes weaker on the mouth bar (Fig. 5g). The amplitudes of the M2 component of the flow velocity increases while the M4 decreases, and the magnitude weakens upstream (Fig. S8a-S8b). As a result, the tidal asymmetry weakens and the phase difference also weakens (Fig. 5h).

4.4 Variations in cumulative water discharge

Modeled monthly cumulative water discharges at the two upstream transects display a similar increasing trend (Fig. 6a-6b). At WT 1, under four constant runoff scenarios, the final cumulative discharge after one month reaches 4.68×10^{10} m^3, 9.24×10^{10} m^3, 13.89×10^{10} m^3 and 18.56×10^{10} m^3, respectively (Fig. 6a; Table S2). At WT 2, with an increase in runoff, both the cumulative discharge and the relative ratio with respect to WT 1 increase (Fig. 6b; Table S2). However, at WT 3 the cumulative discharge is negative in the $Q_{20,000}$ scenario, indicating landward net water movement (Fig. 6c). Under higher runoff, the cumulative discharge is always positive, but the curves show fluctuations during tidal cycles (Fig. 6c). These results highlight that with extreme floods in the flood season more terrestrial materials will enter the SP and then will be transported to the subaqueous delta (Fig. 6; Table S2).

4.5 Geomorphic changes triggered by the 2016 extreme floods

Herein, the hydrodynamics during the 2016 flood season (May and July) were also modeled according to daily riverine water discharge at Datong to determine the impact of extreme floods in the SP. From May to July 2016, the modeled monthly mean bed shear stress increased within the entire SP, the increase gradually weakens seaward, which presents the spatially elongated patterns toward offshore area (Fig. 7a). Therefore, in the inner estuarine channel the mean increase is the highest at 0.044 N/m^2, still as high as 0.040 N/m^2 in shallower mouth bar, while it reduces to 0.016 N/m^2 in offshore area (Fig. 7a).

After the peaks in discharge in 2016, net erosion occurred across the SP. Connected erosion patches were generated in the inner reaches upstream of the deltaic mouth bar, especially in the deep main channel (Fig. 7b). After the bar crest, the magnitude of erosion reduces and some deposition patches form. Within the three divided sub-reaches, the mean magnitude is 19.97 cm, 12.21 cm and 4.62 cm, corresponding to a net erosion of 31.63×10^6 m^3, 18.24×10^6 m^3 and 14.50×10^6 m^3, respectively (Fig. 7b).

The relationship between variation in mean shear stress and bathymetric change is shown in Fig. 7c, and is divided into four quadrants. The 70.14% of the area is characterized by an increase in bed shear stress with geomorphic erosion, especially in the deepest and shallowest areas (Fig. 7c). In addition, 28.92% of the area experiences deposition despite enhanced bed shear stresses, with deposit thickness limited to 0.3 m (Fig. 7c). Overall, the 99.06% of the total area is characterized by an increase in bed shear stress, mainly concentrated in the interval of 0-0.05 N/m^2 (Fig. 7d).

70.68% of the area suffers erosion between 0-25 cm, while the deposition area only accounts for 29.32% of the total area with a magnitude of 0-10 cm (Fig. 7e). Extreme floods in 2016 triggered high bed shear stress along the upstream channel, where the greatest erosion occurred with elongated spatial patterns, the shear stress and erosion weakened in the offshore area (Fig. 7e).

Along the thalweg near the South Jiangya Shoal (between km 0 and 6), the mean shear stress increases slightly less, while the erosion gradually becomes stronger and reaches a maximum of 0.49 m (Fig. 8a). The mean shear stress in the inner estuarine channel augments sharply with a stable difference of 0.08 N/m^2, resulting in strong bathymetric erosion (Fig. 8a). On the mouth bar, the mean shear stress increases less, leading to a change from erosion to deposition after the crest (Fig. 8a). In the offshore area, the shear stress increases even less, triggering strong deposition in areas adjacent to the mouth bar; however areas under erosion are present here with varying magnitude (Fig. 8a). A large increase in mean bed shear stress generates more erosion (Fig. 8b-8d).

In the offshore area the magnitude of geomorphic change is small and some deposition occurs (Fig. 8e).

5. Discussion

5.1 Enhanced hydrodynamics under extreme riverine floods

In mega estuarine deltas, hydrodynamic interactions between river input and tidal forcing are complex, especially after extreme riverine floods (Godin, 1999; Zhang et al., 2018a). High runoff dissipates tidal energy and generate large sediment fluxes (Uncles, 2002; Hoitink et al., 2017). In the Yangtze Delta, seaward advection dominates the transport of water along deltaic distributaries, while tidal pumping is stronger in offshore areas (Yun, 2004). Similar hydrodynamics also develop in the distributaries of the Amazon, Apalachicola and Westerschelde Delta, although the effect of extreme floods have received less attention in these systems (Wang et al., 2002; Canestrelli et al., 2010; Leonardi et al., 2015; Asp et al., 2018). In the Yangtze Delta, tides are more asymmetrical in the offshore area under high runoff, but during the dry season tidal distortion is stronger in upstream reaches (Lu et al., 2015; Zhang et a., 2018a; Yu et al., 2020). Moreover, the monsoons runoff inevitably affect residual water levels and promote circulation in the MTZ (Carballo et al., 2009; Song and Wang, 2013).

During the flood season, more runoff with high SSC is funneled into the Yangtze Delta and delivered offshore (Chen et al., 1999; Yun, 2004). Riverine extreme floods can trigger drastic variations in fluvial-tidal hydrodynamics, particularly in inner estuarine channels. In the $Q_{80,000}$ scenario, extreme riverine floods cause higher mean water level and larger water surface gradients within upstream reaches, while tidal forcing in the offshore area is more restricted (Fig. 3a, 4a and 5a). Strong flow velocities and bed shear stresses are generated in the upper channel, while their magnitude is moderate in the offshore area (Fig. 3a-3f, 4a-4f and 5a-5f). Tidal asymmetry of water levels is also enhanced by extreme riverine floods, while velocity asymmetry weakens (Fig. 5g). In addition, variations in tidal skewness indicates that ebb duration is also enlarged under extreme riverine runoff, and the transition from negative to positive skewness gradually migrates toward the crest of the mouth bar (Fig. 9).

High runoff directly causes greater ebb velocity and duration, which are crucial for the strength and direction of residual currents (Dyer 1973; Matte et al., 2019). Under extreme floods, Euler residual currents in the SP are strengthened, especially during spring tides (Fig. 10). In the $Q_{80,000}$ scenario, the residual velocity is about 0.41 m/s in the mid channel, and strengthens to 0.83 m/s toward the tail of the Jiuduansha Shoal (Fig. 10). A significant increase in residual current will inevitably impact sediment budgets, and trigger bathymetric variations at different water depths (Fig. 10 and 7b). In addition, during a riverine flood the DNCP and adjacent reclaimed areas enhance velocity and tidal asymmetry (Liu et al., 2011; Song and Wang; 2013), stratification within the MTZ also increases, which further affect sediment capture (McLachlan et al., 2017; Li et al., 2018).

5.2 Sediment transports driven by extreme riverine floods

Sediment dynamics in mega deltas are variable and are affected by mixing, circulation, tidal pumping and flocculation. All these processes are directly associated to sediment sources and to the relative strength of runoff with respect tidal forcing (Wolanski et al., 1995; Harris et al., 2005; Bolla Pittaluga et al. 2014). During slack water period plenty of fine-grained sediment settles in the delta within the MTZ, particularly if the river is in flood (Hamblin, 1989). Tide pumping and Stokes drift restrict sediment transport seaward, while extreme floods can amplify ebb-dominated transport downstream (Edmonds and Slingerland 2010; Do et al., 2020). In the Gironde Estuary, riverine sediment export mainly occurred in the flood season, and the MTZ location moved downstream thus enhancing sediment resuspension (Sottolichio and Castaing, 1999; van Maanen and Sottolichio, 2018). Brown and Davies (2010) showed that ebb-dominant currents in the Dyfi Estuary, UK, enhanced the downstream transport of river sediment. In the Mekong Delta, a large amount of river sediment was delivered under high runoff to tidal reaches and its subaqueous delta (Thanh et al., 2017;

McLachlan et al. 2017). Hale et al. (2019) also showed that higher runoff significantly increased the duration and amount of sediment transported downstream in lower Ganges-Brahmaputra Delta.

In the Yangtze Delta, after riverine runoff and sediments are delivered in the SP, flow velocity declines due to downstream channel widening and the blocking effect of tidal forcing (Yun, 2004). Meanwhile, salt-fresh water mixing and flocculation are enhanced, so that fine-grained sediments are deposited and develops the mouth bar (Shi et al., 2006; Hu et al., 2009). Fig. 11 shows vertical SSC during a spring tide in September 2017. The SSC on the mouth bar and in the core area of the MTZ is much higher than the SCC in the inner channel and offshore area. This reflects the transport of suspended sediment downstream and the trapping effect of the mouth bar. Liu et al. (2011) also observed that there is a circulation structure in the MTZ where fine-grained sediments are captured in the North Passage, and the riverine water controls estuarine geomorphic evolution through sediment transport and enhanced ebb-dominated residual sediment export. During the flood season or extreme riverine floods, more terrestrial-sourced suspended sediments are delivered to the subaqueous delta.

Furthermore, the grain size and erodibility of bed sediments directly affect the geomorphic adjustment during extreme floods. In the Yangtze Delta, the mouth bar and subaqueous delta are fully developed, and can then provide new eroded sediments (Chen et al., 1999; Yun, 2004). In the upstream SP channel bed sediments are the coarsest (FS2 site), with a mean and median grain size of 0.14 mm and 0.13mm (Table S4). In the offshore area within the MTZ the grain size becomes gradually finer (Table S4). Moreover, modeled mean bed shear stress generated under extreme riverine floods are higher than the critical shear stress for erosion, therefore the inner estuarine channel and parts of the mouth bar will be eroded significantly. The time interval with shear stress higher than the critical one also increase, augmenting erosion (Dai et al., 2015; Luan et al., 2017; Qiao et al., 2021). In the offshore area the bed shear stresses decrease, and more suspended load or eroded bed sediments delivered by ebb-dominated tides will deposit here (Milliman et al., 1985; Li et al., 2019).

5.3 Morphological change triggered by extreme flood

Longitudinal bathymetric changes can reflect hydrodynamic variations and sediment transport (Carriquiry and Sánchez, 1999; Angamuthu et al., 2018). The proportion of Yangtze discharge flowing through the SP has gradually increased to 26% in the past three decades (Dai et al., 2015; Wei et al., 2019). Thus, the upstream part of the SP is suffering from regular erosion, and the superposition of ebb tide and high runoff during the flood season accelerates this process. Our model results show that monthly mean bed shear stress significantly increased during the 2016 extreme floods, especially along inner estuarine channel, reaching a value of 0.036-0.051 N/m^2 (Fig. 12a-12b). The increase in bed shear stress peaks upstream of the crest of the mouth bar, and then weakens downstream moving offshore (Fig. 12b). The magnitude of upstream erosion is also the strongest in the South Jiangya Shoal and mouth bar, despite some fluctuations (Fig. 12c-12d). In the offshore area, the increase in bed shear stress and the bathymetric erosion are lower, and the bed sediments are finer, except for areas where the shoals' isobaths protrude towards the deep channel (Fig. 12c-12d).

In the SP most water discharge is delivered through the main deltaic channel, a small fraction is transported southward along the Nanhui Shoal due to the Coriolis force, and strong northward residual current is also present in the Jiuduansha Shoal (Chen et al., 1999; Yun, 2004). Therefore, hydrodynamic conditions a cause different morphodynamic response in the deep channel and on the fringing shoals (Fig. 12e-12f). Mean bed shear stress is increasing going from the shallow shoals to the deep channel, except for area with a depth between -9 m and -11 m (along the inner estuarine channel) (Fig. 12e). Bathymetric changes are different in areas shallower or deeper than -6 m, the erosion magnitude first weakens and then augments, the latter has a smaller slope (Fig. 15f). The sand fraction decreases moving offshore and exceeds the silt fraction in the deep channel (Fig. S9). Overall, the deep channels are strongly eroded by the 2016 floods, and also the shoals experience large-scale erosion despite the lower increase in bed shear stress (Fig. 12e-12f). Canestrelli et al. (2010) found that tidal currents were concentrated in the deep channels during neap tide along the lower Fly River and its delta, but were uniformly distributed throughout delta during a spring flood tide. Ralston et al. (2013b) reported high flow velocity and bed shear stresses during the late part of the ebb tide, this flow caused sediment erosion in shallow areas. On a long-term scale, Luan et al. (2016) indicated that deposition turned into erosion in the upstream channels of the Yangtze Delta. Erosion mainly occurred in areas with a water depth between -5 and -15 m.

Moreover, it is necessary to determine whether sediments eroded under extreme riverine floods can be fully or partially replenished in the subsequent dry season. To this end, we analyzed seasonal changes in bottom elevation. The SP suffered net erosion with different magnitude in different flood seasons, while net deposition occurred in the following dry seasons except for 2013. The depositing during the dry season was always less than the erosion in the flood season (Fig. 13). Erosion during the flood season occurred along the inner estuarine channel and where the isobaths of the Jiuduansha Shoal protruded toward the deeper channel (Fig. 13a-13d). During the dry season, deposition occurred on the mouth bar or in the upstream channel, while erosion mainly happened in the offshore area and in the downstream part of the channel (Fig. 13a-13d). We need to emphasize that the drastic decrease in sediment load from the watershed is triggering short-term irreversible erosion in the upstream reaches of the channel; this erosion is more prominent during periods of high runoff (Yang et al., 2014; Dai et al., 2018; Mei et al., 2021).

Historically, riverine floods have controlled the geomorphic evolution of the Yangtze Delta. After the 1954 riverine floods, the Tongsha Shoal was cut by high runoff and gradually morphed into a bifurcation, creating the North Passage and South Passage (Yun, 2004). The 1983 extreme floods continued to deeply cut the upstream shoal and generated the South Jiangya Shoal, the 1998 extreme floods together with the implementation of the DNCP reconnected the South Jiangya Shoal and Jiuduansha Shoal, restoring the SP into a single channel (Yun, 2004). Morphodynamic responses are the natural consequence of large water and sediment fluxes into estuarine deltas. River floods sometimes accelerate channels migration, such as in the Sittaung River Estuary, Myanmar (Choi et al., 2020). Nones et al. (2020) modeled hydro-morphodynamics in the Po River Delta, Italy, during the 2009 flood, highlighting the impact on deltaic morphology.

5.4 Implications for the evolution of mega deltas

Extreme riverine floods cause higher water levels, augment sediment transport, and reduce tidal fluxes in the lower reaches; therefore, whether on a short- or long-term scale, flood processes inevitably impact the evolution of deltaic systems (Zăinescu et al., 2019; Olliver et al., 2020). Seaward Euler residual transport is driven by high runoff; the coupling of sediment convergence and landward density-driven flow develops the MTZ (Hamblin, 1989; Azhikodan and Yokoyama, 2019; Matte et al., 2019). In the SP the MTZ is partly developed and abundant deposition has favored the growth of a mouth bar (Fig. 14a).

In the flood season, high bed shear stresses occur and erode riverbed sediment in inner estuarine channel. This significantly increases SSC and the total sediment load (Fig. 14b). However, during the dry season the riverine regime weakens, and tidal forcing and landward directed bed shear stresses increase in the offshore area. As a result, some sediments are eroded and transported landward toward the mouth bar and upstream channel (Fig. 14c). Historical satellite images indicate that the SSC in the inner estuarine channel greatly increased and the sediment plume expanded downstream after large-scale floods in 1998, 2016 and 2020 (Fig. S10).

In the future, the riverine sediment supply from the Yangtze River will be limited, the rate of accumulation will be reduced, and strong erosion will occur around the -10 m isobath; all these processes will pose new challenges to delta progradation and development (Yang et al., 2011; Dai et al., 2014; Zhu et al., 2016). High bed shear stress caused by extreme riverine floods can suspend more marine sediment in the Yangtze Delta, these sediment might alleviate the erosion caused by insufficient terrestrial sources of sediment (Dai et al., 2018; Wang et al., 2020; Yang et al., 2020; Leonardi et al., 2021). Since the last century, most mega deltas are experiencing erosion and overall geomorphologic disequilibrium caused by inadequate sediment supply, sea level rise, and human disturbances (Syvitski and Saito, 2007; Anthony et al., 2015; Duc Tran et al., 2018). We urgently need to understand sediment redistribution in tidal reaches and deltaic distributaries to predict the evolution of deltas in a period of accelerated sea level rise.

6. Conclusions

Nowadays deltas are threatened by insufficient sediment supply and rising sea levels. Deltaic hydrodynamics and morphodynamics are dominated by riverine inputs and tidal forcing. The non-linear feedbacks between these two processes are complex and regulate the evolution of the system. However, how sediment-poor riverine floods impact the sediment budgets of mega deltas is not well understood. Herein, we combined field data and Delft 3D model simulations to study the hydrodynamics and bathymetry changes in the South Passage, the largest distributary of the Yangtze Delta, after the 2016 riverine floods. Our main conclusions are the following:

(1) Extreme floods triggered higher water levels, flow velocities and bed shear stresses along the deep estuarine channel and on the mouth bar, while the magnitude of hydrodynamic enhancement in the offshore area is limited. At the same time, the proportion of water discharge flowing into the SP increase during the floods.

(2) During extreme floods, the amplitude of the M2 and M4 tidal constituents of water level were reduced and enlarged, respectively, resulting in a greater tidal asymmetry. The Euler residual current thus strengthened and generated faster ebb velocity and a longer duration of the ebb flow.

(3) During the 2016 extreme floods, the transport capacity of riverine suspended and eroded bed sediments was significantly increased, therefore, net erosion occurred. The mean eroded thickness was 19.97 cm in inner estuarine channel and weakened to 12.21 cm and 4.62 cm on the mouth bar and offshore area, respectively.

(4) Hydro-morphodynamics triggered by extreme floods varied as a function of water depth and in different sub-reaches. From shower shoals to deep channel, the mean bed shear stress caused by extreme floods increase going from shallow shoals to the

deep channel, while the mean erosion was the smallest between the -5 m and -6 m isobath. In addition, local topography (South Jiangya Shoal and crest of mouth bar) also contributed to erosion-deposition patterns.

The extreme riverine floods of 2016 delivered more sediment to offshore areas. Under the superimposed pressures from insufficient sediments supply and relative sea level rise, sediment-poor floods will alleviate erosion in mega fluvial-tidal delta.

Declaration of Competing Interest

The authors declare that they have no known competing financial interests or personal relationships that could have appeared to influence the work reported in this paper.

Acknowledgments

This study was financially supported by the Joint Key Funds of National Natural Science Foundation of China (U2040202), the Fundamental Research Funds for the Central Universities and ECNU Academic Innovation Promotion Program for Excellent Doctoral Students (YBNLTS2019-008). Sergio Fagherazzi was partly funded by the USA National Science Foundation award 1637630 (PIE LTER) and 1832221 (VCR LTER).

References

Allen, J. I., Somerfield, P. J., & Gilbert, F. J. (2007). Quantifying uncertainty in high-resolution coupled hydrodynamic-ecosystem models. Journal of Marine Systems, 64(1-4), 3-14.

Allison, M. A., Weathers III, H. D., & Meselhe, E. A. (2017). Bottom morphology in the Song Hau distributary channel, Mekong River delta, Vietnam. Continental Shelf Research, 147, 51-61. https://doi.org/10.1016/j.csr.2017.05.010

Angamuthu, B., Darby, S. E., & Nicholls, R. J. (2018). Impacts of natural and human drivers on the multi-decadal morphological evolution of tidally-influenced deltas. Proceedings of the Royal Society A, 474(2219), 20180396.

Anthony, E. J., Brunier, G., Besset, M., Goichot, M., Dussouillez, P., & Nguyen, V. L. (2015). Linking rapid erosion of the Mekong River delta to human activities. Scientific reports, 5(1), 1-12.

Asp, N. E., Gomes, V. J. C., Schettini, C. A. F., Souza-Filho, P. W. M., Siegle, E., Ogston, A. S., Nittrouer, C. A., Silva, J. N. S., Nascimento, W. R., Souza, S. R., Pereira, L. C. C., Queiroz, M. C. (2018). Sediment dynamics of a tropical tide-dominated estuary: Turbidity maximum, mangroves and the role of the Amazon River sediment load. Estuarine, Coastal and Shelf Science, 214, 10-24.

Azhikodan, G., & Yokoyama, K. (2019). Seasonal morphodynamic evolution in a meandering channel of a macrotidal estuary. Science of The Total Environment, 684, 281-295.

Best, J. (2019). Anthropogenic stresses on the world's big rivers. Nature Geoscience, 12(1), 7-21.

Bianchi, T. S., & Allison, M. A. (2009). Large-river delta-front estuaries as natural "recorders" of global environmental change. Proceedings of the National Academy of Sciences, 106(20), 8085-8092.

Bolla Pittaluga, M., Tambroni, N., Canestrelli, A., Slingerland, R., Lanzoni, S., & Seminara, G. (2015). Where river and tide meet: The morphodynamic equilibrium of alluvial estuaries. Journal of Geophysical Research: Earth Surface, 120(1), 75-94.

Boudet, L., Sabatier, F., & Radakovitch, O. (2017). Modelling of sediment transport pattern in the mouth of the Rhone delta: Role of storm and flood events. Estuarine, Coastal and Shelf Science, 198, 568-582.

Brown, J. M., & Davies, A. G. (2010). Flood/ebb tidal asymmetry in a shallow sandy estuary and the impact on net sand transport. Geomorphology, 114(3), 431-439

Changjiang Water Resources Commission (CWRC), 2019. Changjiang River Sediment Bulletin. Wuhan, China: Changjiang Press. (in Chinese)

Canestrelli, A., Fagherazzi, S., Defina, A., & Lanzoni, S. (2010). Tidal hydrodynamics and erosional power in the Fly River delta, Papua New Guinea. Journal of Geophysical Research: Earth Surface, 115(F4).

Carballo, R., Iglesias, G., & Castro, A. (2009). Residual circulation in the Ria de Muros (NW Spain): a 3D numerical model study. Journal of Marine Systems, 75(1-2), 116-130.

Carriquiry, J. D., & Sánchez, A. (1999). Sedimentation in the Colorado River delta and Upper Gulf of California after nearly a century of discharge loss. Marine Geology, 158(1-4), 125-145.

Chen, J. Y., Yun, C. X., Xu, H. G., & Dong, Y. F. (1979). The developmental model of the ChangJiang River estuary during last 2000 years. Acta Oceanologica Sinica, 1, 103–111 (in Chinese with English abstract).

Chen, J. Y., Li, D. J., Chen, B. L., Hu, F. X., Zhu, H. F., & Liu, C. Z. (1999). The processes of dynamic sedimentation in the Changjiang Estuary. Journal of Sea Research, 41(1-2), 129-140.

Choi, K., Kim, D., & Jo, J. (2020). Morphodynamic evolution of the macrotidal Sittaung River estuary, Myanmar: Tidal versus seasonal controls. Marine Geology, 430, 106367.

Chu, A. (2019). Analysis and modelling of Morphodynamics of the Yangtze Estuary (Doctoral dissertation, Delft University of Technology).

Cooper, J. A. G. (2002). The role of extreme floods in estuary-coastal behaviour: Contrasts between river-and tide-dominated microtidal estuaries. Sedimentary Geology, 150(1-2), 123-137.

Dai, Z. J., & Liu, J. T. (2013). Impacts of large dams on downstream fluvial sedimentation: An example of the Three Gorges Dam (TGD) on the Changjiang (Yangtze River). Journal of Hydrology, 480, 10-18.

Dai, Z. J., Chu, A., Li, W. H., Li, J. F., & Wu, H. L. (2013). Has suspended sediment concentration near the mouth bar of the Yangtze (Changjiang) Estuary been declining in recent years? Journal of Coastal Research, 29(4), 809-818.

Dai, Z., Fagherazzi, S., Mei, X., Gao, J. (2016). Decline in suspended sediment concentration delivered by the Changjiang (Yangtze) River into the East China Sea between 1956 and 2013. Geomorphology, 268, 123-132.

Dai, Z., Liu, J. T., Wei, W., Chen, J. (2014). Detection of the Three Gorges Dam influence on the Changjiang (Yangtze River) submerged delta. Scientific Reports, 4(1), 1-7.

Dai, Z. J., Liu, J. T., & Wen, W. (2015). Morphological evolution of the south passage in the Changjiang (Yangtze River) estuary, China. Quaternary International, 380, 314-326.

Dai, Z. J., Mei, X. F., Darby, S. E., Lou, Y. Y, & Li, W. H. (2018). Fluvial sediment transfer in the Changjiang (Yangtze) river-estuary depositional system. Journal of hydrology, 566, 719-734.

Dai, Z. J., Du, J. Z., Tang, Z. H., Ou, S. Y., Brody, S., Mei, X. F., Jing. J. T., Yu, S. B. (2019). Detection of linkage between solar and lunar cycles and runoff of the world's large rivers. Earth and Space Science, 6(6), 914-930.

Dalrymple, R. W., & Choi, K. (2007). Morphologic and facies trends through the fluvial–marine transition in tide-dominated depositional systems: a schematic framework for environmental and sequence-stratigraphic interpretation. Earth-Science Reviews, 81(3-4), 135-174.

Darby, S. E., Hackney, C. R., Leyland, J., Kummu, M., Lauri, H., Parsons, D. R., Best, J., Nicholas, A.P., Aalto, R. (2016). Fluvial sediment supply to a mega-delta reduced by shifting tropical-cyclone activity. Nature, 539(7628), 276-279.

Deltares. User manual Delft3D-Flow: Simulation of multi-dimensional hydrodynamic flows and transport phenomena, including sediments. Version 3.15, Delft, Netherlands. 2014.

Do, A. T., Sottolichio, A., Huybrechts, N., & Gardel, A. (2020). Circulation patterns and implication for fine sediment transport in a preserved tropical estuary: The case of the Maroni (French Guiana). Regional Studies in Marine Science, 40, 101493.

Duc Tran, D., Halsema, G. V., Hellegers, P. J., Phi Hoang, L., Quang Tran, T., Kummu, M., & Ludwig, F. (2018). Assessing impacts of dike construction on the flood dynamics of the Mekong Delta. Hydrology and Earth System Sciences, 22(3), 1875-1896.

Dyer, K. R. (1973). Estuaries: a physical introduction. Wiley-Interscience, New York and London.

Edmonds, D. A., & Slingerland, R. L. (2010). Significant effect of sediment cohesion on delta morphology. Nature Geoscience, 3(2), 105-109.

Fagherazzi, S., Edmonds, D. A., Nardin, W., Leonardi, N., Canestrelli, A., Falcini, F., Jerolmack D.J., Mariotti, G., Rowland, J.C., Slingerland, R.L. (2015). Dynamics of river mouth deposits. Reviews of Geophysics, 53(3), 642-672.

Fan, D. D., Wu, Y. J., Zhang, Y., Burr, G., Huo, M., & Li, J. (2017). South Flank of the Yangtze Delta: Past, present, and future. Marine Geology, 392, 78-93.

Fettweis, M., Sas, M., & Monbaliu, J. (1998). Seasonal, neap-spring and tidal variation of cohesive sediment concentration in the Scheldt Estuary, Belgium. Estuarine, Coastal and Shelf Science, 47(1), 21-36.

Friedrichs, C. T., & Aubrey, D. G. (1988). Non-linear tidal distortion in shallow well-mixed estuaries: a synthesis. Estuarine, Coastal and Shelf Science, 27(5), 521-545.

Gerten, D., Rost, S., von Bloh, W., Lucht, W. (2008). Causes of change in 20th century global river discharge. Geophysical Research Letters, 35(20).

Glover, H. E., Ogston, A. S., Fricke, A. T., Nittrouer, C. A., Aung, C., Naing, T., Kyu, K., & Htike, H. (2021). Connecting Sediment Retention to Distributary-Channel Hydrodynamics and Sediment Dynamics in a Tide-dominated Delta: The Ayeyarwady Delta, Myanmar. Journal of Geophysical Research: Earth Surface, 126(3), e2020JF005882.

Godin, G. (1999). The propagation of tides up rivers with special considerations on the Upper Saint Lawrence River. Estuarine, Coastal and Shelf Science, 48(3), 307-324.

Hale, R., Bain, R., Goodbred Jr, S., & Best, J. (2019). Observations and scaling of tidal mass transport across the lower Ganges–Brahmaputra delta plain: implications for delta management and sustainability. Earth Surface Dynamics, 7(1), 231-245.

Hamblin, P. F. (1989). Observations and model of sediment transport near the turbidity maximum of the Upper Saint Lawrence Estuary. Journal of Geophysical Research:

Oceans, 94(C10), 14419-14428.

Harris, C. K., Traykovski, P. A., & Geyer, W. R. (2005). Flood dispersal and deposition by near-bed gravitational sediment flows and oceanographic transport: A numerical modeling study of the Eel River shelf, northern California. Journal of Geophysical Research: Oceans, 110(C9).

Hoitink, A. J. F., & Jay, D. A. (2016). Tidal river dynamics: Implications for deltas. Reviews of Geophysics, 54(1), 240-272.

Hoitink, A. J. F., Wang, Z. B., Vermeulen, B., Huismans, Y., & Kästner, K. (2017). Tidal controls on river delta morphology. Nature geoscience, 10(9), 637-645.

Hu, K. L., Ding, P. X., Wang, Z. B., & Yang, S. L. (2009). A 2D/3D hydrodynamic and sediment transport model for the Yangtze Estuary, China. Journal of Marine Systems, 77(1-2), 114-136.

Kitheka, J. U., Obiero, M., & Nthenge, P. (2005). River discharge, sediment transport and exchange in the Tana Estuary, Kenya. Estuarine, Coastal and Shelf Science, 63(3), 455-468.

Lamb, M. P., Nittrouer, J. A., Mohrig, D., & Shaw, J. (2012). Backwater and river plume controls on scour upstream of river mouths: Implications for fluvio-deltaic morphodynamics. Journal of Geophysical Research: Earth Surface, 117(F1).

Lentz, E. E., & Hapke, C. J. (2011). Geologic framework influences on the geomorphology of an anthropogenically modified barrier island: assessment of dune/beach changes at Fire Island, New York. Geomorphology, 126(1-2), 82-96.

Leonardi, N., Kolker, A. S., & Fagherazzi, S. (2015). Interplay between river discharge and tides in a delta distributary. Advances in Water Resources, 80, 69-78.

Leonardi, N., Mei, X. F., Carnacina, I., & Dai, Z. J. (2021). Marine sediment sustains the accretion of a mixed fluvial-tidal delta. Marine Geology, 106520.

Li, L., He, Z. G., Xia, Y. Z., & Dou, X. P. (2018). Dynamics of sediment transport and stratification in Changjiang River Estuary, China. Estuarine, Coastal and Shelf Science, 213, 1-17.

Li, J. F., & Zhang, C. (1998). Sediment resuspension and implications for turbidity maximum in the Changjiang Estuary. Marine Geology, 148(3-4), 117-124.

Li, Y. M., Zhang, G. A., You, B. W., & Li, Z. H. (2019). Recent sediment characteristics and their impact factors in the Yangtze Estuary riverbed. Acta Geographica Sinica, 74(1), 178-190. (in Chinese with English abstract)

Liu, G. F., Zhu, J. R., Wang, Y. Y., Wu, H., & Wu, J. X. (2011). Tripod measured residual currents and sediment flux: Impacts on the silting of the Deepwater Navigation Channel in the Changjiang Estuary. Estuarine, Coastal and Shelf Science, 93(3), 192-201.

Lu, S., Tong, C. F., Lee, D. Y., Zheng, J. H., Shen, J., Zhang, W., & Yan, Y. X. (2015). Propagation of tidal waves up in Yangtze Estuary during the dry season. Journal of Geophysical Research: Oceans, 120(9), 6445-6473.

Luan, H. L., Ding, P. X., Wang, Z. B., Ge, J. Z., & Yang, S. L. (2016). Decadal morphological evolution of the Yangtze Estuary in response to river input changes and estuarine engineering projects. Geomorphology, 265, 12-23.

Luan, H. L., Ding, P. X., Wang, Z. B., & Ge, J. Z. (2017). Process-based morphodynamic modeling of the Yangtze Estuary at a decadal timescale: Controls on estuarine evolution and future trends. Geomorphology, 290, 347-364.

Maillet, G.M., Vella, C., Berné, S., Friend, P.L., Amos, C.L., Fleury, T.J. Normand, A., (2006). Morphological changes and sedimentary processes induced by the December 2003 flood event at the present mouth of the Grand Rhône River (southern France). Marine Geology, 234(1-4), 159-177.

Matte, P., Secretan, Y., & Morin, J. (2019). Drivers of residual and tidal flow variability in the St. Lawrence fluvial estuary: Influence on tidal wave propagation. Continental Shelf Research, 174, 158-173.

McLachlan, R. L., Ogston, A. S., & Allison, M. A. (2017). Implications of tidally-varying bed stress and intermittent estuarine stratification on fine-sediment dynamics through the Mekong's tidal river to estuarine reach. Continental Shelf Research, 147, 27-37.

Mei, X., Dai, Z., Darby, S. E., Gao, S., Wang, J., & Jiang, W. (2018a). Modulation of extreme flood levels by impoundment significantly offset by floodplain loss downstream of the Three Gorges Dam. Geophysical Research Letters, 45(7), 3147-3155.

Mei, X. F., Dai, Z. J, Wei, W., Li, W. H., Wang, J., & Sheng, H. (2018b). Secular bathymetric variations of the North Channel in the Changjiang (Yangtze) Estuary, China, 1880–2013: Causes and effects. Geomorphology, 303, 30-40.

Mei, X. F., Dai, Z. J., Darby, S. E., Zhang, M., Cai, H. Y., Wang, J., & Wei, W. (2021). Landward shifts of the maximum accretion zone in the tidal reach of the Changjiang estuary following construction of the Three Gorges Dam. Journal of Hydrology, 592, 125789.

Milliman, J. D., Huang-Ting, S., Zuo-Sheng, Y., & Mead, R. H. (1985). Transport and deposition of river sediment in the Changjiang estuary and adjacent continental shelf. Continental Shelf Research, 4(1-2), 37-45.

Nidzieko, N. J. (2010). Tidal asymmetry in estuaries with mixed semidiurnal/diurnal tides. Journal of Geophysical Research: Oceans, 115(C8).

Nienhuis, J. H., Ashton, A. D., Edmonds, D. A., Hoitink, A. J. F., Kettner, A. J., Rowland, J. C., & Törnqvist, T. E. (2020). Global-scale human impact on delta morphology has led to net land area gain. Nature, 577(7791), 514-518.

Nones, M., Maselli, V., & Varrani, A. (2020). Numerical modeling of the hydro-morphodynamics of a distributary channel of the po river delta (Italy) during the spring 2009 flood event. Geosciences, 10(6), 209.

Olliver, E. A., Edmonds, D. A., & Shaw, J. B. (2020). Influence of floods, tides, and vegetation on sediment retention in Wax Lake Delta, Louisiana, USA. Journal of Geophysical Research: Earth Surface, 125(1), e2019JF005316.

Pawlowicz, R., Beardsley, B., & Lentz, S. (2002). Classical tidal harmonic analysis including error estimates in MATLAB using T_TIDE. Computers & Geosciences, 28(8), 929-937.

Qiao, Y., He, Q., & Wang, X. Y. (2021). Experimental study on critical shear stress of surface sediments in the Yangtze Estuary. Sediment Research, 46(01) 34-41. (in Chinese with English abstract)

Ralston, D. K., Warner, J. C., Geyer, W. R., & Wall, G. R. (2013a). Sediment transport due to extreme events: The Hudson River estuary after tropical storms Irene and

Lee. Geophysical Research Letters, 40(20), 5451-5455.

Ralston, D. K., Geyer, W. R., Traykovski, P. A., & Nidzieko, N. J. (2013b). Effects of estuarine and fluvial processes on sediment transport over deltaic tidal flats. Continental Shelf Research, 60, S40-S57.

Shen, H.T., & Pan, D.A. (2001). Turbidity maximum in the Changjiang estuary. China Ocean: Beijing, China. (in Chinese)

Shi, J. Z., Zhang, S. Y., & Hamilton, L. J. (2006). Bottom fine sediment boundary layer and transport processes at the mouth of the Changjiang Estuary, China. Journal of Hydrology, 327(1-2), 276-288.

Sibson, R. (1981). A Brief Description of Natural Neighbor Interpolation. Interpreting Multivariate Data, John Wiley & Sons, New York, 21-36.

Song, D., & Wang, X. H. (2013). Suspended sediment transport in the Deepwater Navigation Channel, Yangtze River Estuary, China, in the dry season 2009: 2. Numerical simulations. Journal of Geophysical Research: Oceans, 118(10), 5568-5590.

Sottolichio, A., & Castaing, P. (1999). A synthesis on seasonal dynamics of highly-concentrated structures in the Gironde estuary. Comptes Rendus de l'Académie des Sciences-Series IIA-Earth and Planetary Science, 329(11), 795-800.

Syvitski, J. P. (2003). Supply and flux of sediment along hydrological pathways: research for the 21st century. Global and Planetary Change, 39(1-2), 1-11.

Syvitski, J. P., & Saito, Y. (2007). Morphodynamics of deltas under the influence of humans. Global and Planetary Change, 57(3-4), 261-282.

Thanh, V. Q., Reyns, J., Wackerman, C., Eidam, E. F., & Roelvink, D. (2017). Modelling suspended sediment dynamics on the subaqueous delta of the Mekong River. Continental Shelf Research, 147, 213-230.

Uncles, R. J. (2002). Estuarine physical processes research: some recent studies and progress. Estuarine, Coastal and Shelf Science, 55(6), 829-856.

van Maanen, B., & Sottolichio, A. (2018). Hydro-and sediment dynamics in the Gironde estuary (France): sensitivity to seasonal variations in river inflow and sea level rise. Continental Shelf Research, 165, 37-50.

van Maren, D. S., & Hoekstra, P. (2004). Seasonal variation of hydrodynamics and sediment dynamics in a shallow subtropical estuary: the Ba Lat River, Vietnam. Estuarine, Coastal and Shelf Science, 60(3), 529-540.

Wang, M., Zheng, H., Xie, X., Fan, D., Yang, S., Zhao, Q., & Wang, K. (2011). A 600-year flood history in the Yangtze River drainage: comparison between a subaqueous delta and historical records. Chinese Science Bulletin, 56(2), 188-195.

Wang, J., Dai, Z. J., Mei, X. F., & Fagherazzi, S. (2020). Tropical Cyclones Significantly Alleviate Mega-Deltaic Erosion Induced by High Riverine Flow. Geophysical Research Letters, 47(19), e2020GL089065.

Wang, Z. B., Jeuken, M. C. J. L., Gerritsen, H., De Vriend, H. J., & Kornman, B. A. (2002). Morphology and asymmetry of the vertical tide in the Westerschelde estuary. Continental Shelf Research, 22(17), 2599-2609.

Wei, W., Dai, Z. J., Mei, X. F., Gao, S., & Liu, J. P. (2019). Multi-decadal morpho-sedimentary dynamics of the largest Changjiang estuarine marginal shoal: Causes and implications. Land Degradation & Development, 30(17), 2048-2063.

Wolanski, E., King, B., & Galloway, D. (1995). Dynamics of the turbidity maximum in the Fly River estuary, Papua New Guinea. Estuarine, Coastal and Shelf Science, 40(3), 321-337.

Wu, J. X., Liu, J. T., & Wang, X. (2012). Sediment trapping of turbidity maxima in the Changjiang Estuary. Marine Geology, 303, 14-25.

Yang, H. F., Yang, S. L., Xu, K. H., Wu, H., Shi, B. W., Zhu, Q., Yang, Z. (2017). Erosion potential of the Yangtze Delta under sediment starvation and climate change. Scientific reports, 7(1), 1-12.

Yang, S. L., Milliman, J. D., Li, P., & Xu, K. (2011). 50,000 dams later: erosion of the Yangtze River and its delta. Global and Planetary Change, 75(1-2), 14-20.

Yang, S. L., Milliman, J. D., Xu, K. H., Deng, B., Zhang, X. Y., & Luo, X. X. (2014). Downstream sedimentary and geomorphic impacts of the Three Gorges Dam on the Yangtze River. Earth-Science Reviews, 138, 469-486.

Yang, S. L., Luo, X., Temmerman, S., Kirwan, M., Bouma, T., Xu, K., Zhang, S. S., Fan, J. Q., Shi, B. W., Yang, H. F., Wang, Y. P., Shi, X. F., & Gao, S. (2020). Role of delta-front erosion in sustaining salt marshes under sea-level rise and fluvial sediment decline. Limnology and Oceanography, 65(9), 1990-2009.

Yu, X. Y., Zhang, W., & Hoitink, A. J. F. (2020). Impact of river discharge seasonality change on tidal duration asymmetry in the Yangtze River Estuary. Scientific reports, 10(1), 1-17.

Yun, C. X. (2004). Basic Law of the Recent Evolution of the Changjiang Estuary. Beijing, China Ocean Press. (in Chinese)

Zăinescu, F., Vespremeanu-Stroe, A., Anthony, E., Tătui, F., Preoteasa, L., & Mateescu, R. (2019). Flood deposition and storm removal of sediments in front of a deltaic wave-influenced river mouth. Marine Geology, 417, 106015.

Zhang, F. Y., Sun, J., Lin, B. L., & Huang, G. X. (2018a). Seasonal hydrodynamic interactions between tidal waves and river flows in the Yangtze Estuary. Journal of Marine Systems, 186, 17-28.

Zhang, M., Townend, I., Cai, H. Y., He, J., Mei, X. F. (2018). The influence of seasonal climate on the morphology of the mouth-bar in the Yangtze Estuary, China. Continental Shelf Research, 153, 30-49.

Zhang, X. H., Fagherazzi, S., Leonardi, N., & Li, J. F. (2018b). A positive feedback between sediment deposition and tidal prism may affect the morphodynamic evolution of tidal deltas. Journal of Geophysical Research: Earth Surface, 123(11), 2767-2783.

Zhou, X., Dai, Z., Mei, X. (2020). The multi-decadal morphodynamic changes of the mouth bar in a mixed fluvial-tidal estuarine channel. Marine Geology, 429, 106311.

Zhu, L., He, Q., Shen, J., & Wang, Y. Y. (2016). The influence of human activities on morphodynamics and alteration of sediment source and sink in the Changjiang Estuary. Geomorphology, 273, 52-62.

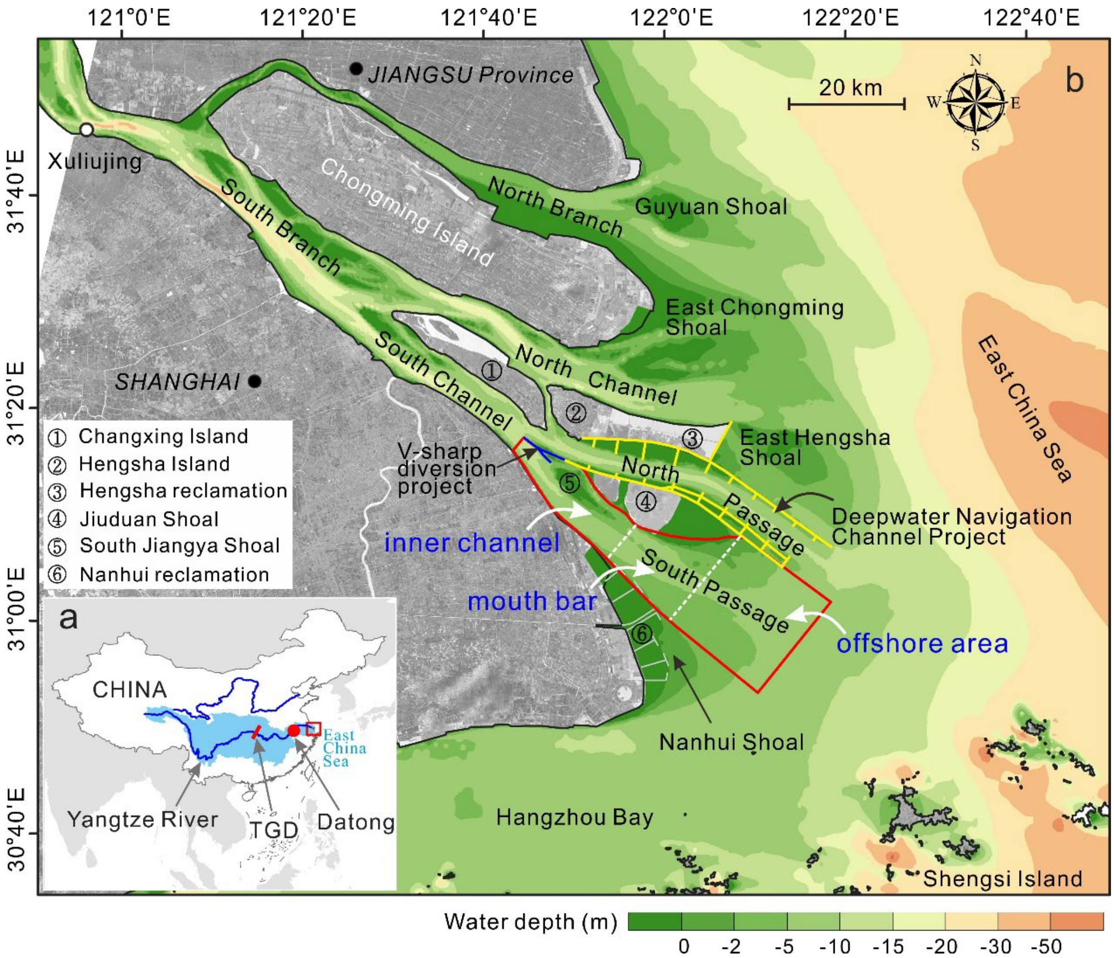

Fig. 1. Map of the Yangtze River Basin and Delta. (a) The Yangtze River Basin is located in the subtropical monsoon zone of central-southern China. The Three Gorges Dam (TGD) and Datong hydrological station (tidal limit) are also shown. (b) The three-order distributary system of the Yangtze Delta. The South Passage (SP) is indicated with a red polygon. A month bar and lateral shoals are present in the SP. The channel is longitudinally divided into three sub-reaches: the inner estuarine channel, the mouth bar and the offshore area.

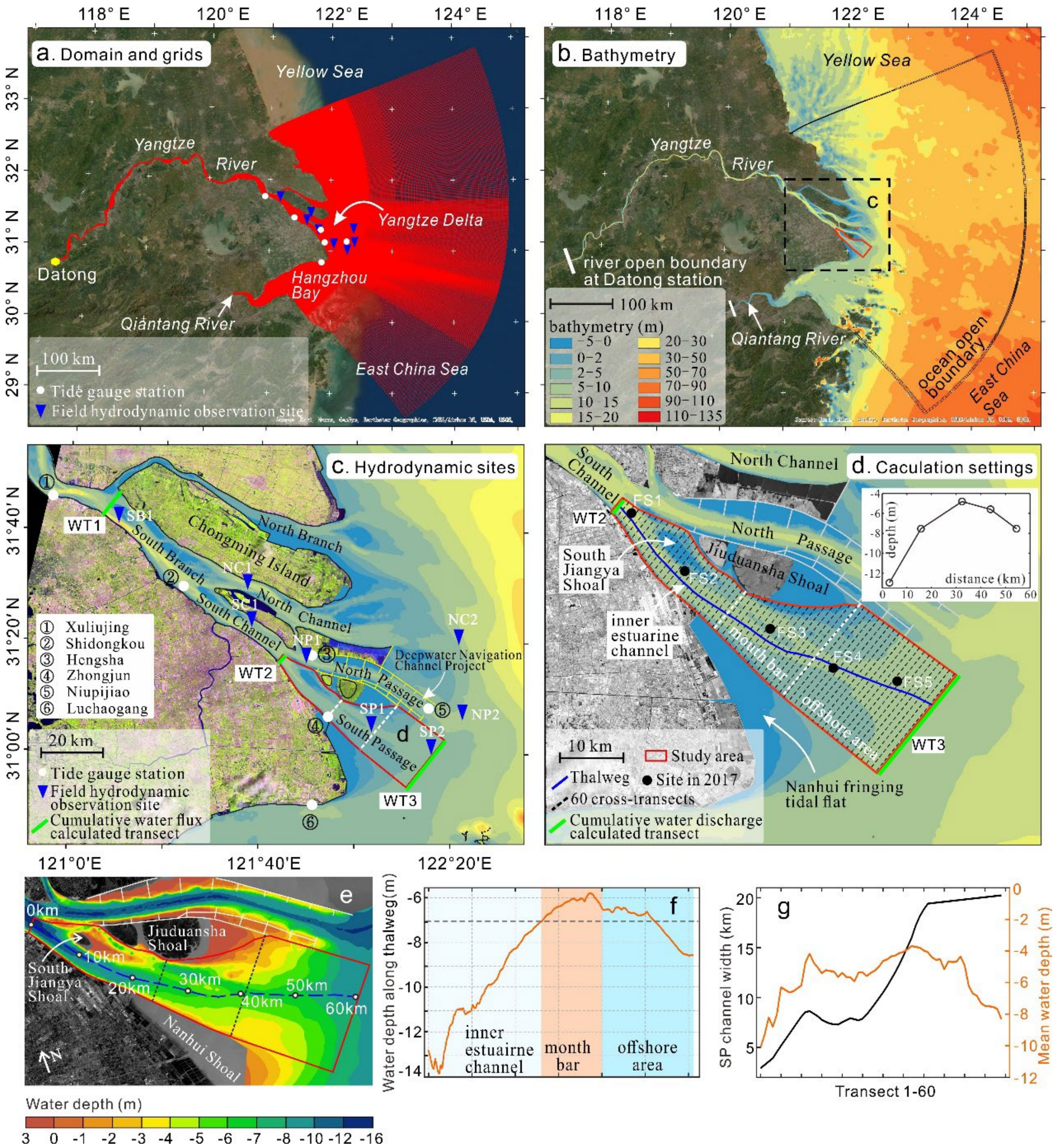

Fig. 2. (a) Prescribed model domain and grids, showing the tide gauge stations (white points) and hydrodynamic observation sites (blue triangles). (b) Bathymetry of the Yangtze Delta and surrounding areas, the riverine boundary in Datong and the ocean open boundary are indicated. (c) Hydrodynamic sites used for calibration. Three transects (WT 1, WT 2 and WT 3, green solid lines) were set up to calculate cumulative water fluxes during the entire modeled period. (d) Transects used for hydrodynamic and geomorphic analyses, including thalweg (blue solid line) and 60 equally spaced cross-sections (black dotted lines); the five black dots indicate hydrological observation stations in September 2017. (e) Bathymetry in May 2016 and the location of thalweg (dots represent intervals of 10 km), the three sub-reaches of the SP are also shown. (f) Longitudinal water depth along the thalweg. (g) Channel width and mean water depth of 60 cross-transects.

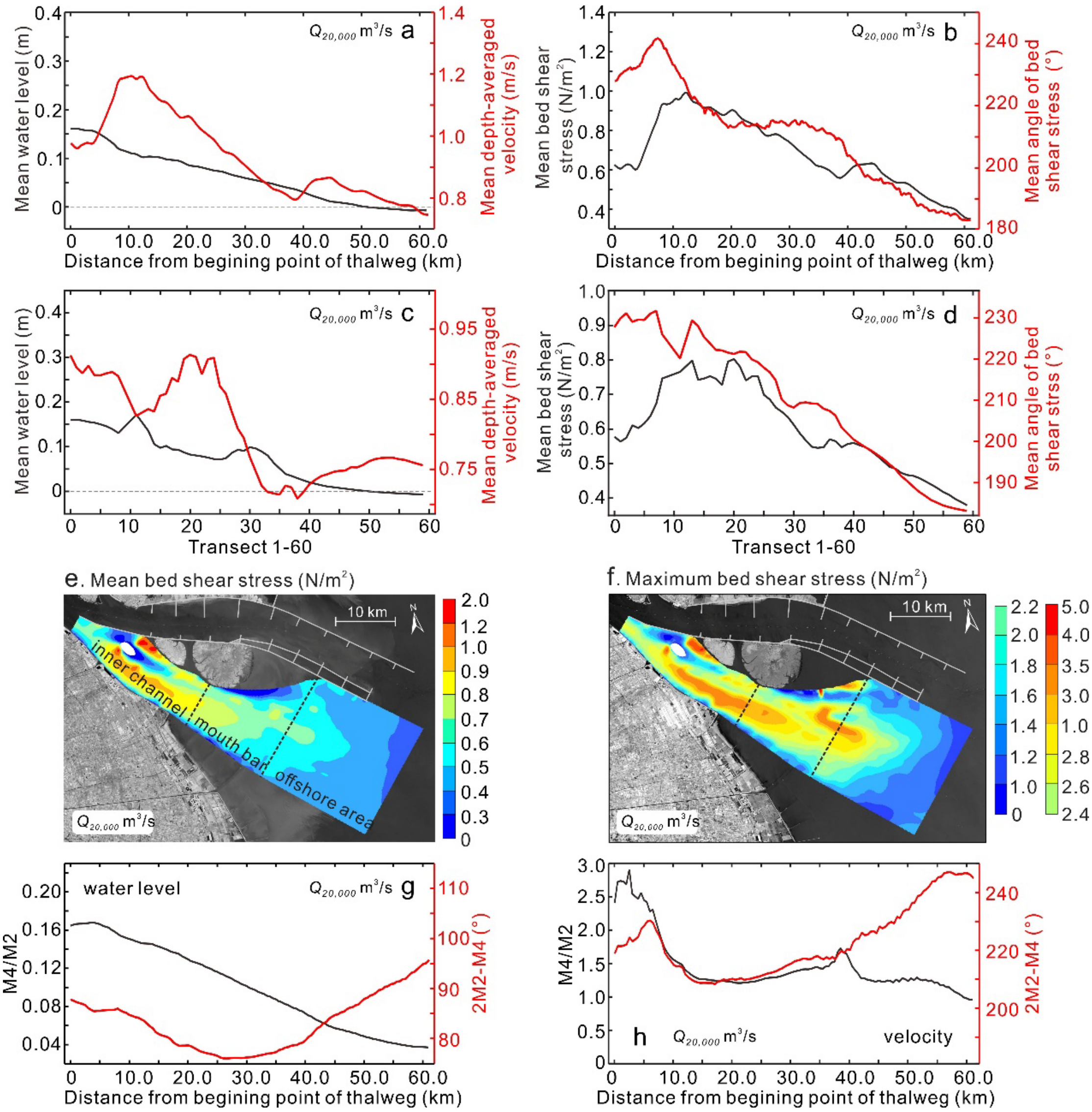

Fig. 3. *Q20,000* scenario: the longitudinal variations in modeled (a) mean water level and mean depth-averaged water velocity, (b) mean bed shear stress and its angle, extracted along the thalweg. (c-d) Modeled hydrodynamic variables averaged over the 60 cross sections. (e-f) Modeled mean and maximum bed shear stress in the SP. (g-h) Amplitude ratio of M4 to M2 constituents and corresponding phase difference (2M2-M4) of modeled water level and velocity.

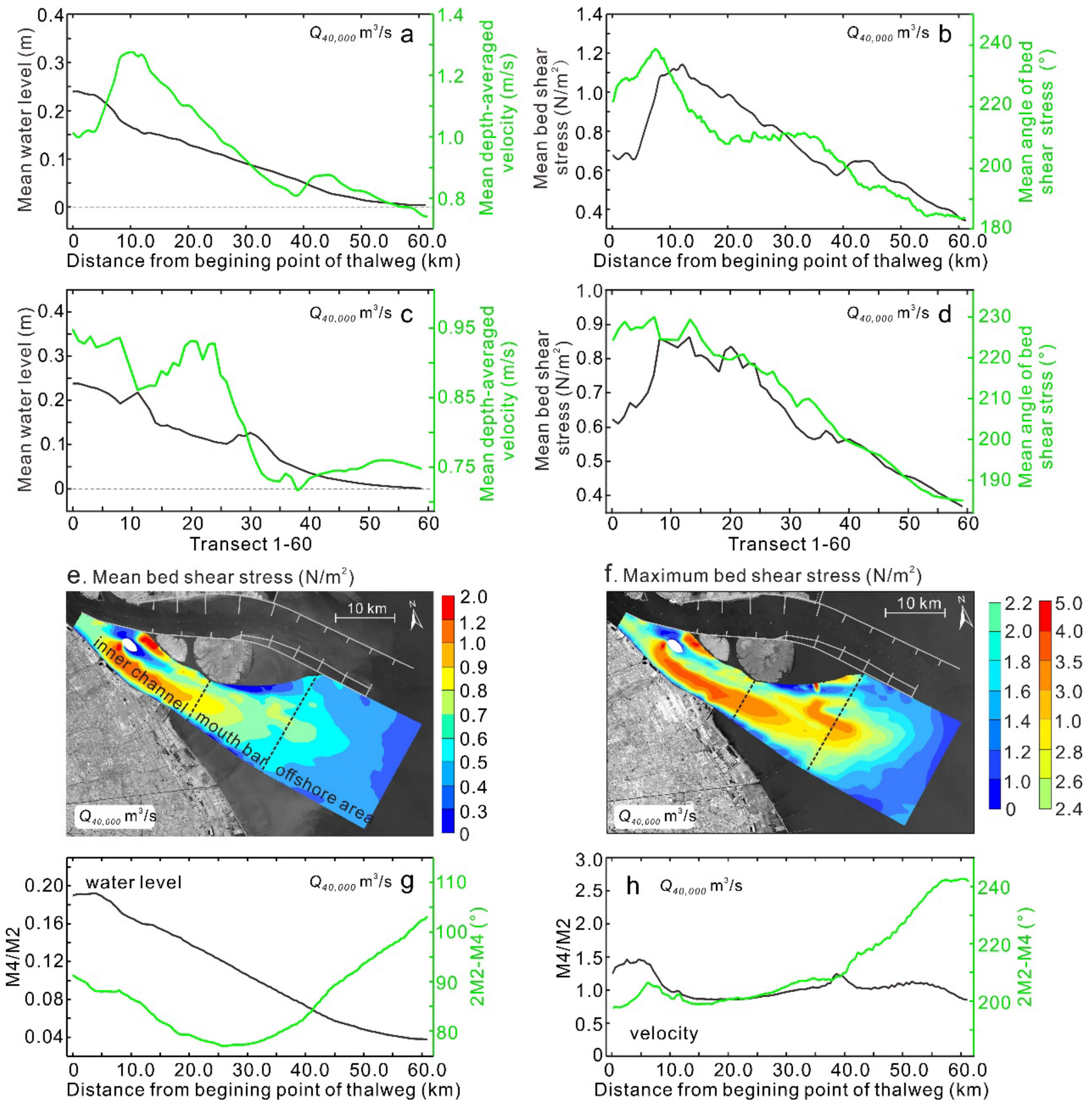

Fig. 4. *$Q_{40,000}$* scenario: longitudinal variations in modeled (a) mean water level and depth-averaged water velocity, (b) mean bed shear stress and its angle extracted along the thalweg. (c-d) Modeled hydrodynamic variables averaged over the 60 cross sections. (e-f) Modeled mean and maximum bed shear stress in the SP. (g-h) Amplitude ratio of M4 to M2 constituents and corresponding phase difference (2M2-M4) of modeled water level and velocity.

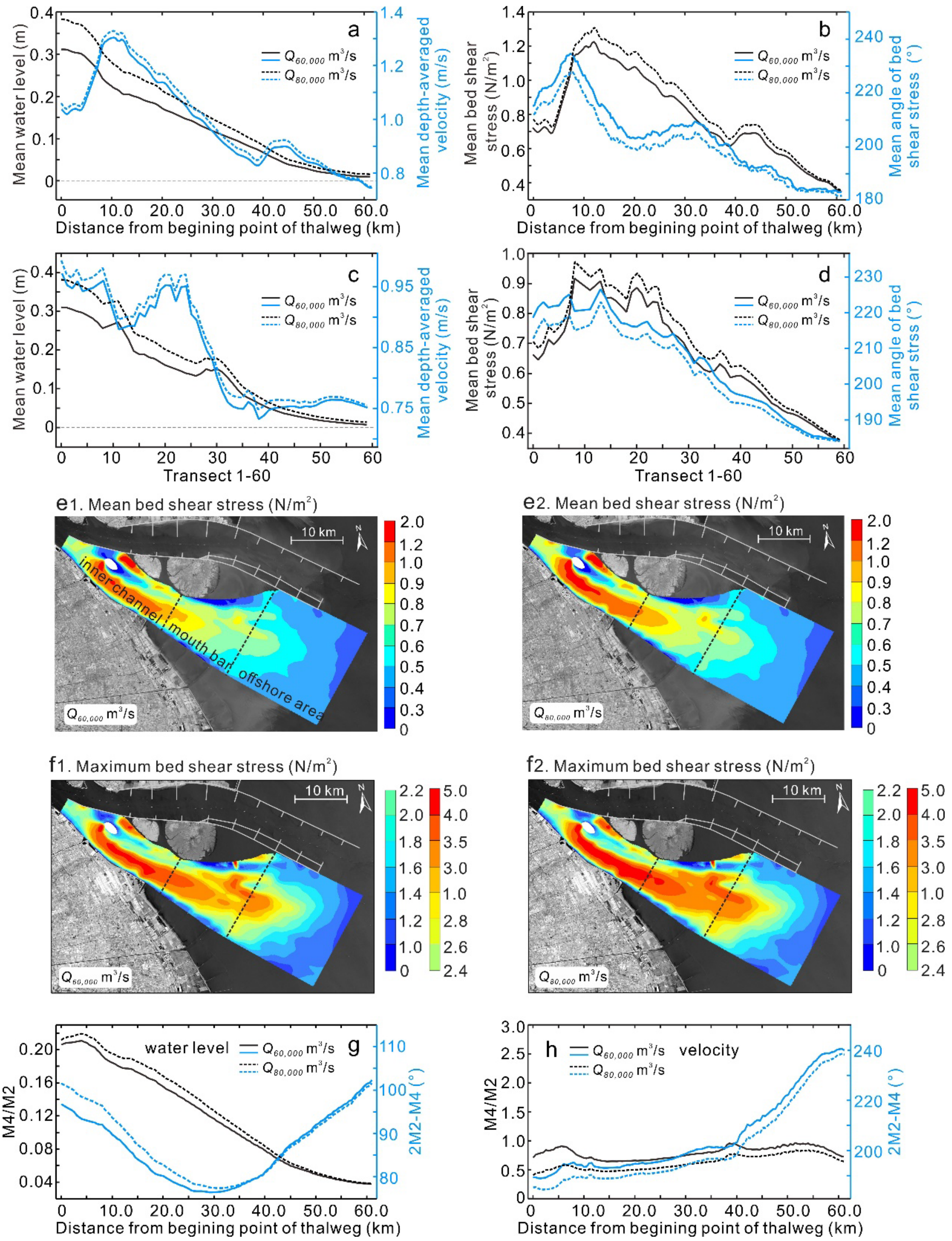

Fig. 5. $Q_{60,000}$ and $Q_{80,000}$ scenarios: longitudinal variations in modeled (a) mean water level and depth-averaged water velocity, (b) mean bed shear stress and its angle extracted along the thalweg. (c-d) Modeled hydrodynamic variables averaged over the 60 cross sections. (e-f) Modeled mean and maximum bed shear stress in the SP. (g-h) Amplitude ratio of M4 to M2 constituents and corresponding phase difference (2M2-M4) of modeled water level and velocity.

.

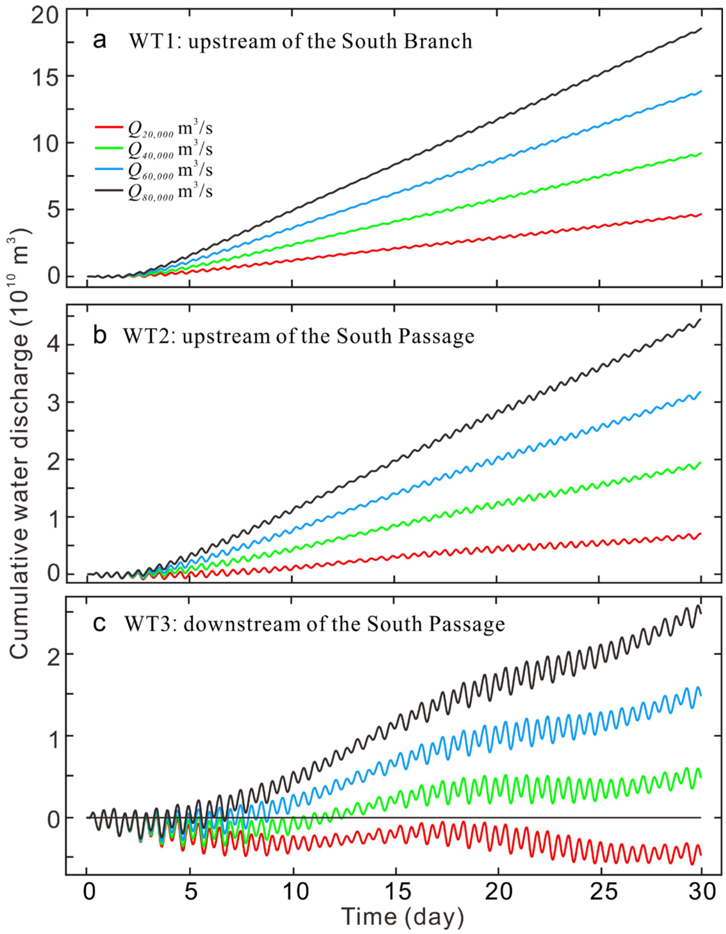

Fig. 6. Cumulative water discharge through three monitoring transects in four model scenarios, (a) transect WT1, (b) transect WT2 and (c) transect WT3.

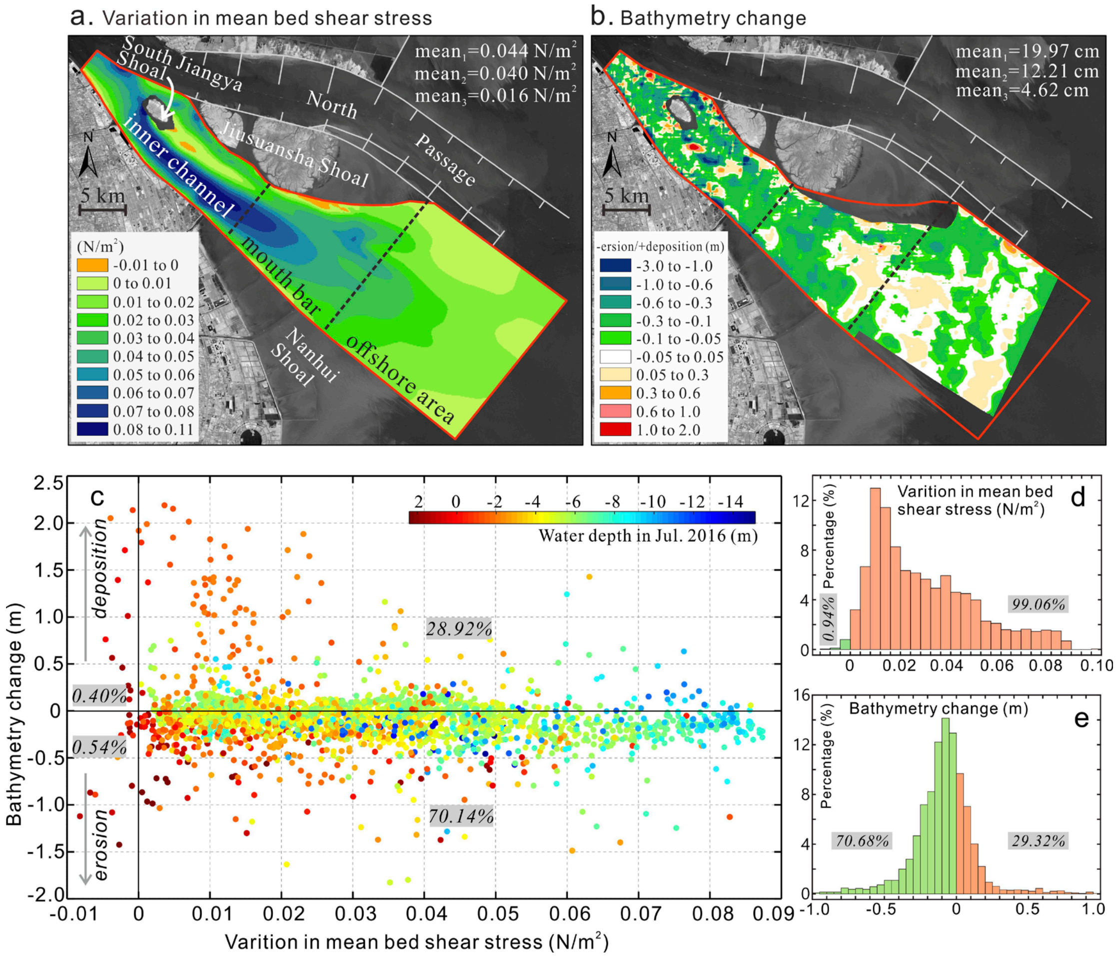

1064 **Fig. 7.** (a) Modeled difference in mean bed shear stress between low flow $Q_{20,000}$ and
1065 high flow $Q_{80,000}$ conditions and (b) change in measured bathymetry from May 2016 to
1066 early August 2016 in the SP. (c) Relationship between bed shear stress and bathymetric
1067 change divided in four quadrants, the colormap indicates water depth in July 2016. (d-
1068 e) Frequency distributions of bed shear stress difference and bathymetric change.
1069

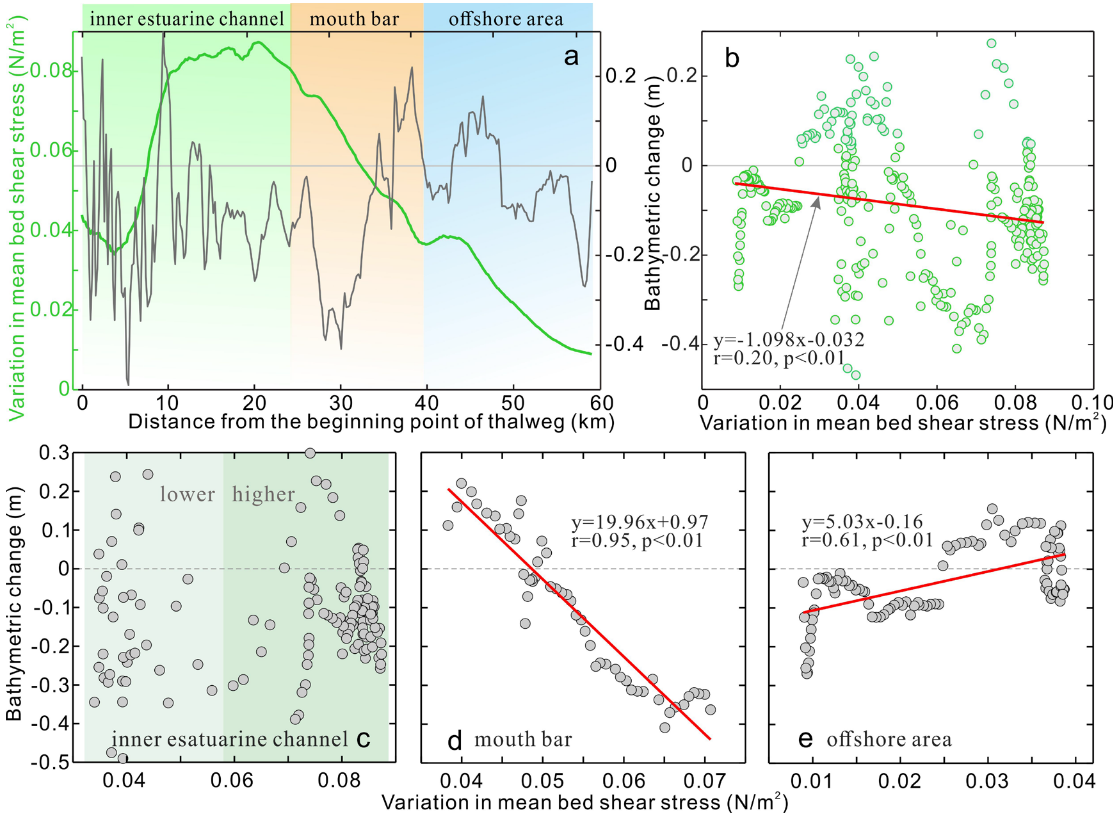

Fig. 8. (a) Longitudinal variations in mean bed shear stress and bathymetry along the thalweg from May 2016 to early August 2016. Relationship between shear stress variation from low flow to high flow and bathymetric change (b) in the entire SP, (c) in the inner estuarine channel, (d) on the mouth bar and (e) in offshore area.

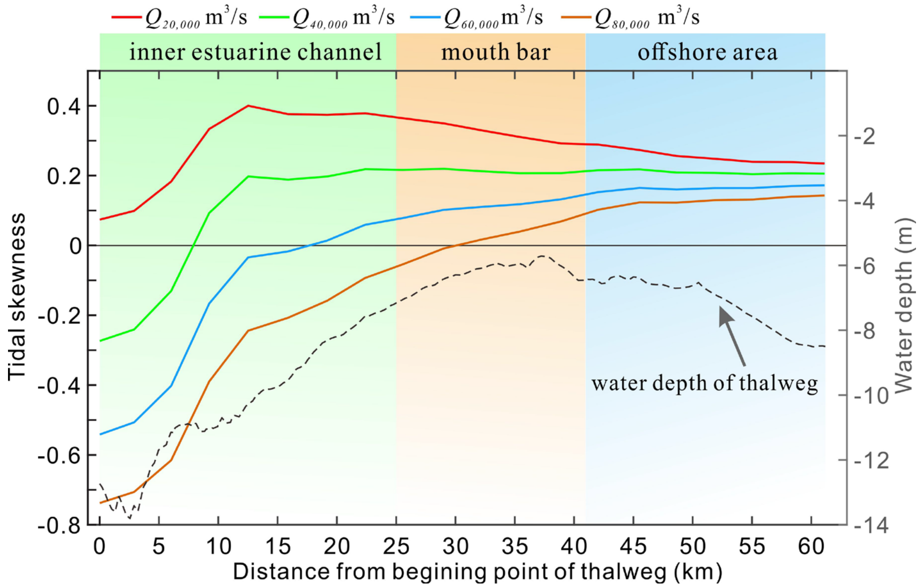

1077 **Fig. 9.** Tidal skewness along the thalweg and water depth in four modeled scenarios.

1078

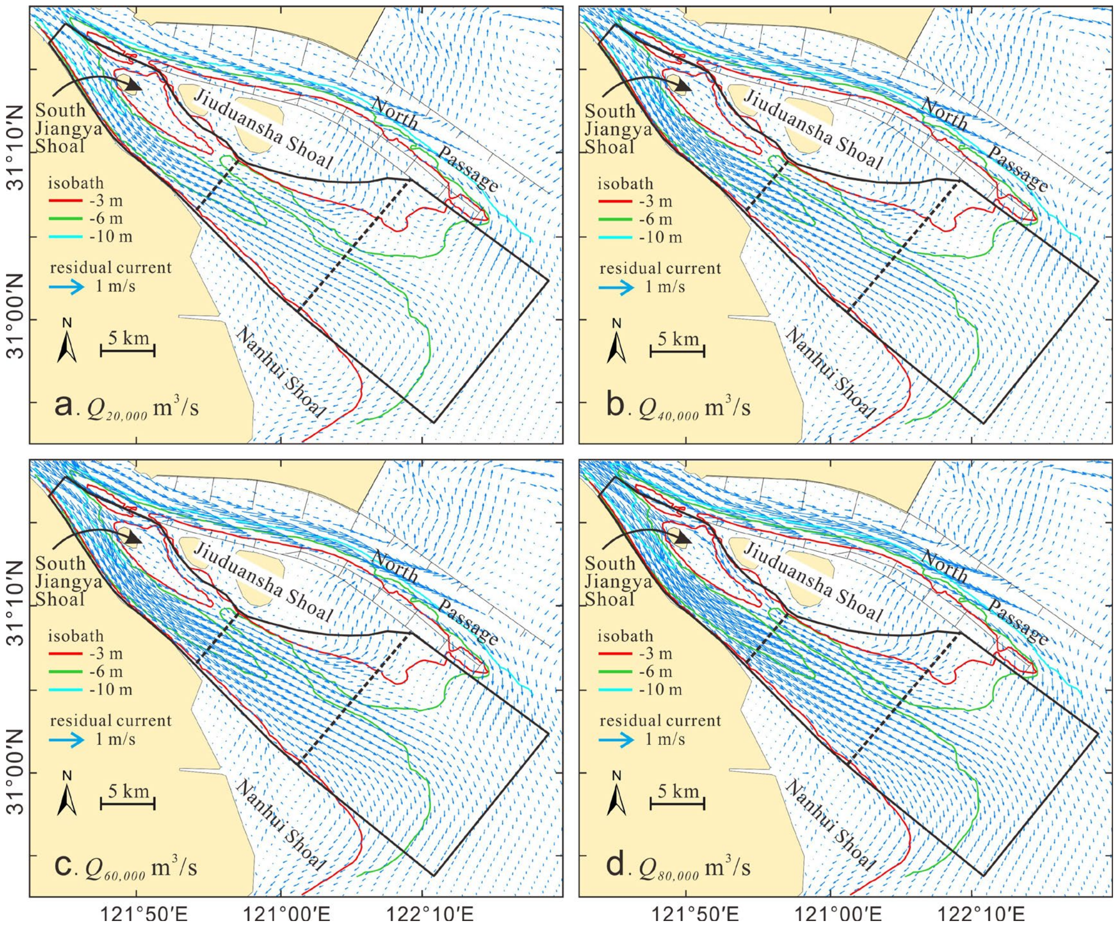

1080 **Fig. 10.** Residual velocities in spring tide for the scenarios (a) $Q_{20,000}$, (b) $Q_{40,000}$, (c)
1081 $Q_{60,000}$ and (d) $Q_{80,000}$, the isobaths and the three sub-reaches are also indicated.

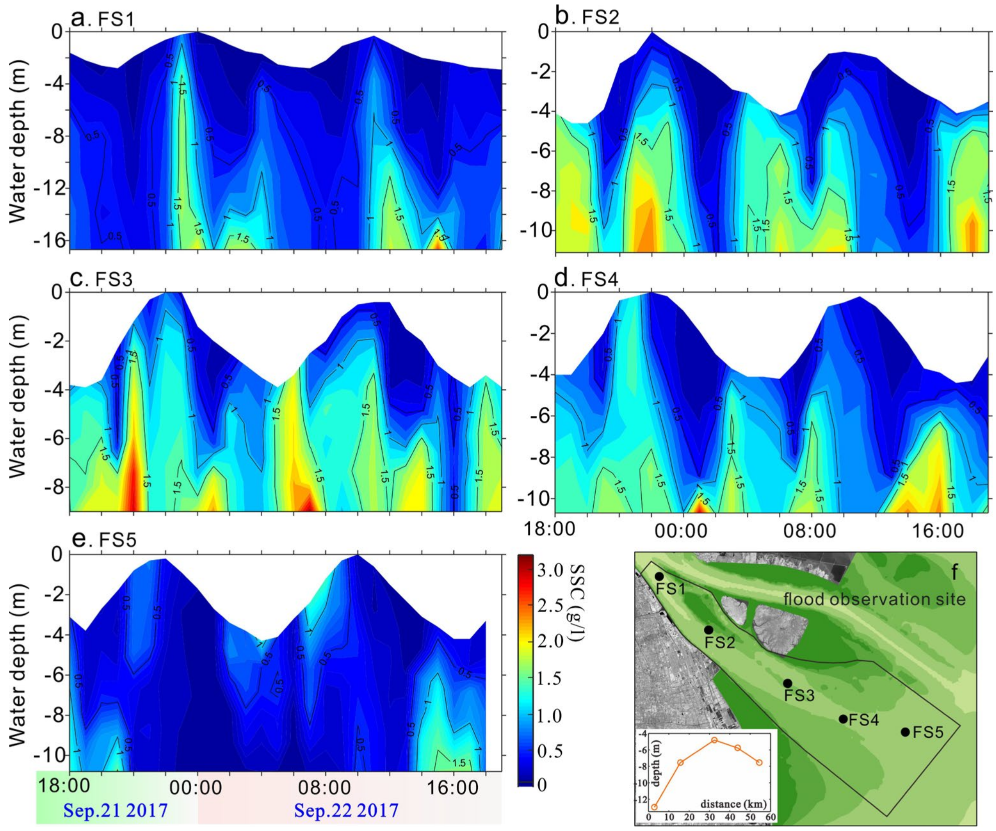

1083 **Fig. 11.** (a-e) Vertical SSC during spring tide at five sites, the measurements were synchronously taken in the 2017 flood season. (f) Location and water depth of the five sites.

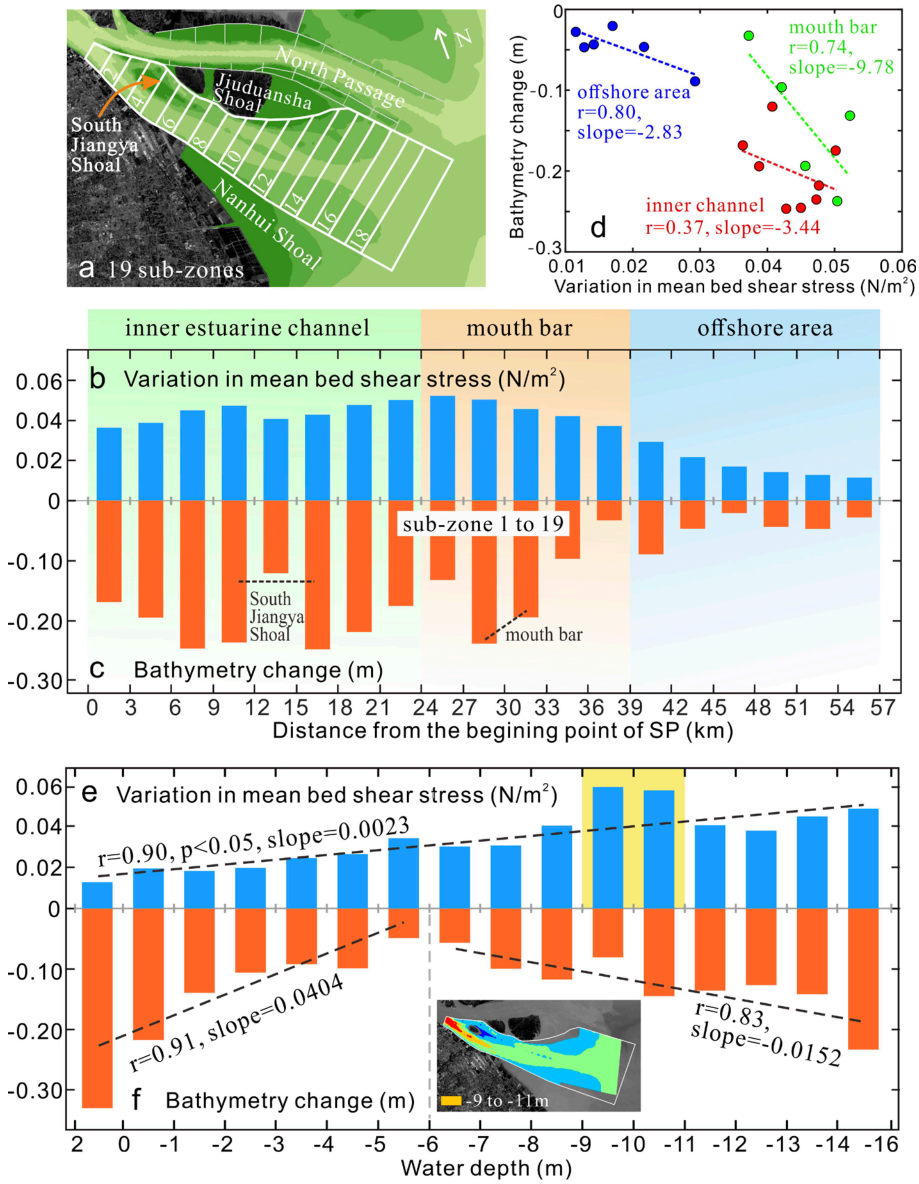

1087 **Fig. 12.** (a) 19 sub-zones in the SP, (b-d) mean variations in average bed shear stress
1088 and bathymetric change in the sub-zones, and (e-f) mean variations in average bed shear
1089 stress and bathymetric change at different water depths.

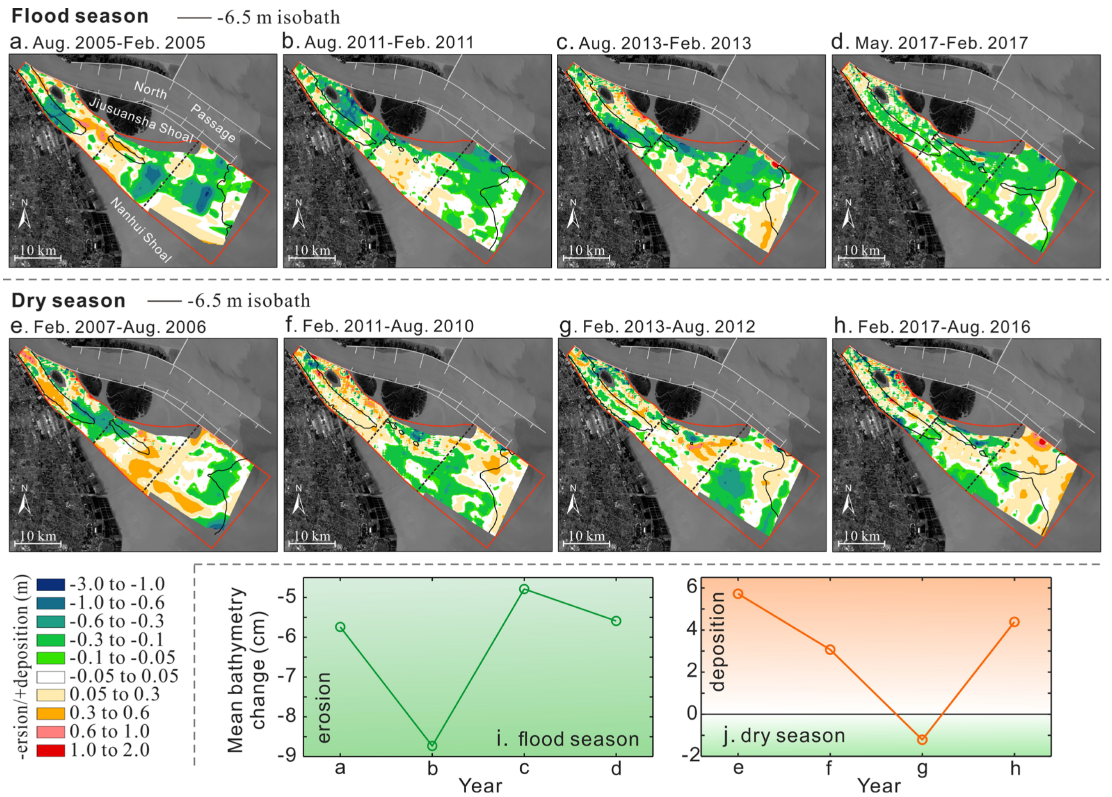

Fig. 13. Historical geomorphological changes during (a-d) flood season and (e-h) subsequent dry season. the -6.5 m isobath in each subgraph corresponds to the earlier bathymetry. (i-j) mean thickness of erosion (negative) and deposition (positive) during different periods.

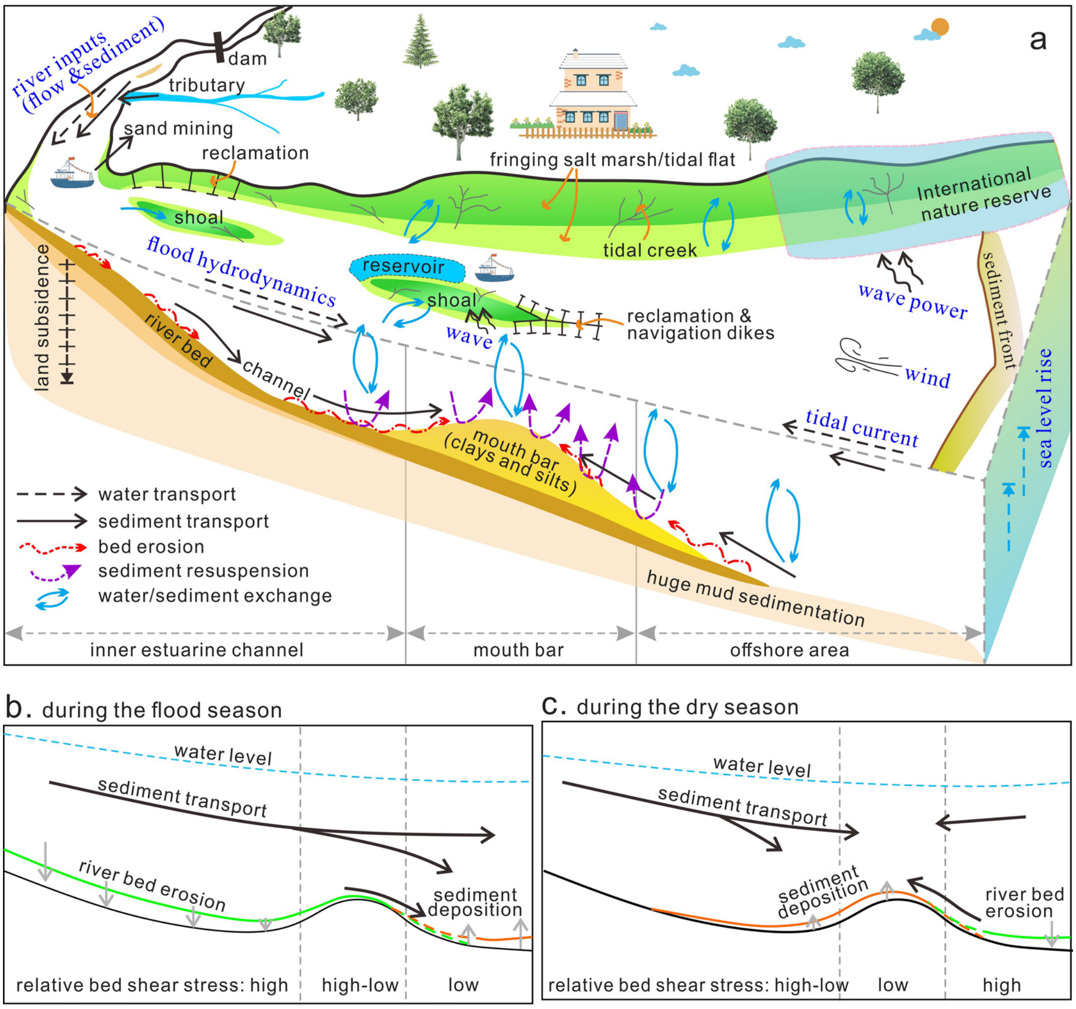

1096 **Fig. 14.** (a) Schematic diagram of hydrodynamics, sediment transports and geomorphic characters of channel-shoal-mouth bar system in the Yangtze Delta. (b-c) Longitudinal water level and riverbed erosion-deposition distribution during the flood season and dry season respectively under current terrestrial sediment supply.